UNIVERSIDADE
BEIRA INTERIOR

Experimental Study of a Plunging NACA0012 Airfoil under Asymmetric Oscillations

(versão final após defesa)

Joana Gomes Santos Silva

Dissertação para obtenção do Grau de Mestre em
Engenharia Aeronáutica
(Ciclo de estudos integrado)

Orientador: Prof. Doutor André Resende Rodrigues da Silva

abril de 2023

Declaração de Integridade

Eu, Joana Gomes Santos Silva, que abaixo assino, estudante com o número de inscrição 39833 de Engenharia Aeronáutica da Faculdade de Engenharia, declaro ter desenvolvido o presente trabalho e elaborado o presente texto em total consonância com o **Código de Integridades da Universidade da Beira Interior**.

Mais concretamente afirmo não ter incorrido em qualquer das variedades de Fraude Académica, e que aqui declaro conhecer, que em particular atendi à exigida referenciação de frases, extratos, imagens e outras formas de trabalho intelectual, e assumindo assim na íntegra as responsabilidades da autoria.

Universidade da Beira Interior, Covilhã 11/04/2023

Assinado por: **Joana Gomes Santos Silva**
Num. de Identificação: 15941906
Data: 2023.04.11 21:51:13+01'00'

Dedicatória

”Aqueles que passam por nós não vão sós. Deixam um pouco de si, levam um pouco de nós.”

Antoine de Saint-Exupéry

Ao meu pai, que sempre me encorajou a seguir os meus sonhos.

Acknowledgments

”Our greatest weakness lies in giving up. The most certain way to succeed is always to try just one more time.”

Thomas Edison

First of all, I would like to thank my supervisor, Professor André Silva, for giving me the opportunity to carry out this work and guiding me throughout it, motivating me always to continue.

To Professor Jorge Barata, for having the opportunity to work in AEROG - Aeronautics and Astronautics Research Center, which provided me with all the material and facilities necessary to accomplish this work.

To FCT (Fundação para a Ciência e Tecnologia), which provided sponsorship through a scholarship in Aeronautical Engineering, under the scope of the project ”Verão com Ciência”.

I also would like to thank all my colleagues at AEROG, who, in more difficult moments, of hard work, allowed everything to continue in the best way. I would especially like to thank Emanuel Camacho and João Pinho for all the help, exchange of ideas and moments well spent in the laboratory, which helped me to always overcome the difficulties in the most positive way possible.

Finally, I would like to thank my family, especially my mother and my brother, for the support they always gave me in all stages of my life. They always believed in me and in my abilities to complete my goals. Thank you very much for all the support and love you have always given me.

Thank you all!

Joana Santos Silva

Resumo

Novos desafios fizeram com que o Homem sentisse a necessidade de procurar na natureza, através da Biomimética, formas de ultrapassar variados problemas. Através da observação das formas de locomoção de animais como pássaros e insetos, surgiu um grande interesse nesta forma de locomoção que permite a simultânea geração de propulsão e sustentação, no que é considerado um regime de baixo número de Reynolds. Esta dissertação tem como principal objetivo o estudo experimental do movimento assimétrico de um perfil NACA0012 em movimento puramente vertical. Também se pretende estudar a influência da amplitude adimensional e da frequência reduzida nos padrões de esteira deste perfil. Por fim, será realizada uma análise da influência da assimetria do movimento, da amplitude adimensional e da frequência reduzida no ângulo de ataque efetivo do perfil. Os testes são realizados num túnel de vento de secção aberta utilizando-se uma máquina de fumo para marcar o escoamento e uma câmara de alta velocidade para captar a esteira do perfil. Todos os testes são realizados com um número de Reynolds de 1×10^4, considerando-se quatro níveis de assimetria, $\zeta = 0.5$, $\zeta = 0.6$, $\zeta = 0.7$ e $\zeta = 0.8$. A amplitude adimensional estudada encontra-se entre 0.125 e 0.5 e a frequência reduzida entre 0.5 e 8. A visualização do escoamento indica que o movimento assimétrico produz simultaneamente tração e sustentação e que o aumento do parâmetro de assimetria torna a vorticidade mais intensa, fazendo com que estes vórtices se formem mais cedo. A amplitude adimensional e a frequência reduzida têm um impacto semelhante. Verifica-se que com o aumento destes parâmetros, os vórtices formam-se mais a montante, sendo que a sua intensidade também aumenta. Relativamente ao ângulo de ataque efetivo, observa-se através dos resultados obtidos, que o aumento destes três parâmetros provoca um aumento neste ângulo, embora de diferentes formas. A separação do escoamento ocorre mais cedo para maiores valores do parâmetro de assimetria e amplitude adimensional.

Palavras-chave

Biomimética, Perfil Oscilante, Cinemática Assimétrica, Vórtices de Bordo de Ataque, Vórtices de Bordo de Fuga

Abstract

The need to overcome new challenges made the human being seek in nature ways to surpass specific problems through Biomimetics. Through the observation of locomotion modes of animals such as birds and insects, a great interest emerged in this form of motion that allows the simultaneous generation of thrust and lift at low Reynolds numbers. This dissertation has the primary objective of exploring experimentally the asymmetric movement of a NACA0012 airfoil in purely vertical motion. It is also intended to study the influence of the nondimensional amplitude and reduced frequency on the wake patterns of the airfoil. Finally, will be performed an analysis of the influence of motion asymmetry, nondimensional amplitude and reduced frequency on the airfoil's effective angle of attack. The tests are carried out in an open-section wind tunnel using a smoke machine to mark the flow and a high-speed camera to capture the airfoil's wake. All tests are performed with a Reynolds number of 1×10^4 and four levels of asymmetry, $\zeta = 0.5$, $\zeta = 0.6$, $\zeta = 0.7$ and $\zeta = 0.8$, are considered. The nondimensional amplitude studied is between 0.125 and 0.5, and the reduced frequency ranges between 0.5 and 8. The visualization of the flow indicates that the asymmetric motion produces both thrust and lift and that increasing the asymmetry parameter makes the vorticity more intense. Furthermore, these vortices form earlier. Nondimensional amplitude and reduced frequency have a similar impact. It is found that vortices form further upstream with the increase of these parameters, and their intensity also increases. Regarding the effective angle of attack, it is observed through the results that the rise of these three parameters causes an increase in this angle. The separation of the flow occurs earlier for higher values of the asymmetry parameter, nondimensional amplitude and reduced frequency.

Keywords

Biomimetics, Flapping Airfoil, Asymmetric Kinematics, Leading Edge Vortices, Trailing Edge Vortices

Contents

1 Introduction **1**

1.1 Motivation and Objectives . . . 1

1.2 Outline . . . 2

2 Literature Review **3**

2.1 Biomimetics . . . 3

2.2 Flapping Motion . . . 6

2.3 Governing Parameters . . . 7

2.3.1 Environmental Parameters . . . 7

2.3.2 Geometric Parameters . . . 7

2.3.3 Kinematics Parameters . . . 7

2.3.4 Performance Parameters . . . 9

2.4 Flapping airfoils . . . 9

2.5 Studies of flapping wings under asymmetric kinematics . . . 14

3 Methodology **19**

3.1 Experimental Setup . . . 19

3.1.1 Wind Tunnel . . . 20

3.1.2 Wing and Supports . . . 20

3.1.3 Smoke Generator . . . 23

3.1.4 Anemometer . . . 23

3.1.5 Motor and Linear Actuator . . . 24

3.1.6 Controller . . . 25

3.1.7 High Speed Camera . . . 25

3.2 Motion Kinematics . . . 26

3.3 Experimental Validation . . . 29

4 Results and Discussion **31**

4.1 Tested Conditions . . . 31

4.2 Influence of the Asymmetry Parameter, ζ . . . 32

4.2.1 Flow Visualization . . . 32

4.2.2 Influence on the effective angle of attack . . . 36

4.3 Influence of the Nondimensional Amplitude, h . . . 37

4.3.1 Flow Visualization . . . 37

4.3.2 Influence off the effective angle of attack . . . 42

4.4 Influence of the Reduced Frequency, k . . . 43

4.4.1 Flow Visualization . . . 43

4.4.2 Influence of the effective angle of attack . . . 48

5 Conclusion **51**

References **53**

A Anexes **61**

A.1 Cases considered 61

List of Figures

2.1 Leonardo da Vinci's "flying machine". 3
2.2 First successful powered flight. 4
2.3 Eastgate Centre. 4
2.4 London Portcullis House. 4
2.5 Council House Two. 5
2.6 Three types of motion in which the flapping motion is divided. 6
2.7 Schematic of foil kinematics. 6
2.8 Knoller and Betz theory describing the propulsion of a flapping wing. 10
2.9 Typical von Kármán vortex street. 10
2.10 Inverted von Kármán vortex street. 11
2.11 Transition from typical to inverted von Kármán vortex street. 12
2.12 Deflected vortex street. 12

3.1 Experimental setup. 19
3.2 Wind Tunnel. 20
3.3 Isometric, top and left views of the projected wing. 21
3.4 Final wing assembly. 21
3.5 Final Wing. 21
3.6 Isometric, bottom, right and front views of the supports connecting the wing to the linear actuator. 22
3.7 Final support. 22
3.8 Wing, supports and linear actuator. 23
3.9 Smoke system. 23
3.10 Anemometer. 24
3.11 Motor and linear actuator used in the experimental tests. 24
3.12 MEXE software. 25
3.13 Controller. 25
3.14 High Speed Camera. 26
3.15 Airfoil kinematics. 27
3.16 Symmetrical motion profile. 28
3.17 Asymmetrical motion profile. 28
3.18 Comparison between the prescribed motion and experimental results. 29

4.1 Motor limits and tested conditions. 32
4.2 Flow visualization of $\zeta = 0.5$, 0.6, 0.7, and 0.8 with $h = 0.125$, and $k = 2$. 33
4.3 Flow visualization of $\zeta = 0.5$, 0.6, 0.7, and 0.8 with $h = 0.25$, and $k = 1$. 34
4.4 Flow visualization of $\zeta = 0.5$, 0.6, 0.7, and 0.8 with $h = 0.5$, and $k = 0.5$. 35
4.5 Effective angle of attack as a function of period fraction, for $h = 0.125$ and $k = 2$. 36
4.6 Effective angle of attack as a function of period fraction, for $h = 0.25$ and $k = 1$. 36

4.7 Effective angle of attack as a function of period fraction, for $h = 0.50$ and $k = 0.50$. 36
4.8 Flow visualization of $h = 0.125$, 0.25, and 0.5 with $\zeta = 0.5$, and $k = 2$. 38
4.9 Flow visualization of $h = 0.125$, 0.25, and 0.5 with $\zeta = 0.6$, and $k = 1$. 39
4.10 Flow visualization of $h = 0.125$, 0.25, and 0.5 with $\zeta = 0.7$, and $k = 1$. 40
4.11 Flow visualization of $h = 0.125$, 0.25, and 0.5 with $\zeta = 0.8$, and $k = 0.5$. 41
4.12 Effective angle of attack as a function of period fraction, for $\zeta = 0.5$ and $k = 2$. 42
4.13 Effective angle of attack as a function of period fraction, for $\zeta = 0.6$ and $k = 1$. 42
4.14 Effective angle of attack as a function of period fraction, for $\zeta = 0.7$ and $k = 1$. 42
4.15 Effective angle of attack as a function of period fraction, for $\zeta = 0.8$ and $k = 0.5$. 42
4.16 Flow visualization of $k = 0.5$, 1, and 2 with $\zeta = 0.5$, and $h = 0.5$. 44
4.17 Flow visualization of $k = 0.5$, 1, and 2 with $\zeta = 0.6$, and $h = 0.25$. 45
4.18 Flow visualization of $k = 0.5$, 1, and 2 with $\zeta = 0.7$, and $h = 0.25$. 46
4.19 Flow visualization of $k = 0.5$, 1, and 2 with $\zeta = 0.8$, and $h = 0.125$. 47
4.20 Effective angle of attack as a function of period fraction, for $\zeta = 0.5$ and $h = 0.50$. 48
4.21 Effective angle of attack as a function of period fraction, for $\zeta = 0.6$ and $h = 0.25$. 48
4.22 Effective angle of attack as a function of period fraction, for $\zeta = 0.7$ and $h = 0.25$. 48
4.23 Effective angle of attack as a function of period fraction, for $\zeta = 0.8$ and $k = 0.125$. 48

List of Tables

4.1 Final summary of the tested conditions. 32

A.1 Analysis of the conditions to be tested. 61

Nomenclature

Re	Reynolds number	–
ρ	Fluid density	$\mathrm{kg \cdot m^{-3}}$
U_∞	Flow velocity	$\mathrm{m \cdot s^{-1}}$
c	Aerodynamic chord	m
μ	Fluid dynamic viscosity	$\mathrm{Pa \cdot s}$
St	Strouhal number	–
f	Motion frequency	Hz
W	Wake length	m
A	Plunging amplitude	m
h	Non-dimensional amplitude	–
k	Reduced frequency	–
α_{eff}	Effective angle of attack	rad
$\dot{y}$	Plunging velocity	$\mathrm{m \cdot s^{-1}}$
α	Angle of attack	rad
A_α	Pitching amplitude	rad
f_α	Pitching frequency	Hz
ϕ	Phase angle between plunging and pitching	rad
C_t	Thrust coefficient	–
C_d	Drag coefficient	–
C_P	Required power coefficient	–
C_l	Lift coefficient	–
$\dot{\alpha}$	Angle of attack rate	$\mathrm{rad \cdot s^{-1}}$
C_m	Moment coefficient	–
y	Airfoil's vertical coordinate	m
T	Plunging period	s
ζ	Plunging cycle asymmetry	–
t_u	Upwards motion time	s
ξ	Dimensionless acceleration	–

List of Acronyms

MAVs	Micro-Air Vehicles
NAVs	Nano-Air Vehicles
NACA	National Advisory Committee for Aeronautics
DARPA	Defense Advanced Research Projects Agency
LEV	Leading-Edge Vortex
TEV	Trailing-Edge Vortex
AEROG	Aeronautics and Astronautics Research Center
3D	Three-dimensional
PLA	Polylactic Acid

Chapter 1

Introduction

This chapter consists of an introduction to the work and is divided into two subsections. The first subsection describes the motivation and objectives that led to the development of this work. The second subsection, the outline section, consists of a description of the dissertation structure.

1.1 Motivation and Objectives

Animals and insects that move in air or water have attracted the interest of humans since early times. These animals have been investigated because of their locomotion system that allows effective thrust and lift generation at low Reynolds number [1]. Low Reynolds number is used in the literature by several researchers, but there is still difficult to define what separates low from high Reynolds numbers. Thus, researchers seek to imitate the flight of these animals to apply the fundamental concepts to several engineering problems.

For many centuries animals moving in air or water have used flapping surfaces as the main mechanism to produce thrust and lift. Biomimetics seek to understand the flight fundamentals of these animals. Thus, there is a great interest in adapting and developing these mechanisms in the production of vehicles with flapping wings. Thus, a great effort has been made to approach propulsion in aviation to these mechanisms, which occupy a special place, as they have been used by various living beings over the years [2]. More recently, some researchers have used Biomimetics to study Micro and Nano Air Vehicles (MAVs/NAVs), which are small vehicles developed to perform a particular mission. The flight capabilities of insects and birds have inspired the creation of MAVs and NAVs, mainly by identifying the basic principles of flight at such low scales. Micro-Air Vehicles were defined by the Defense Advanced Research Projects Agency (DARPA) program as flying vehicles with no dimension larger than $15\,\mathrm{cm}$ [3]. Thus, the study of flapping wings it's not only applied to the creation of small vehicles but also to the study of bigger scale systems such as rotor aerodynamics.

Over the years, several researchers have investigated pitching and plunging motions, separately and combined, to understand the generation of thrust and lift forces [4]. Experimental and numerical work has been carried out using symmetrical kinematics. The asymmetric study of motion has also been used in numerical studies of plunging and pitching combined motions and in the experimental research of pure pitching motions. However, the experimental study of pure plunging asymmetric movements is not a widely discussed topic and still needs a lot of research. Thus, this dissertation has as its primary objective the further

study of plunging airfoils, especially under asymmetric conditions. An experimental analysis of a NACA0012 plunging airfoil will be carried out, being studied the symmetric and asymmetric motions. The impact of the nondimensional amplitude and reduced frequency will also be analysed since these parameters influence the studied motion, hence the flow field.

This work is a continuation of other transient aerodynamics works already carried out at AEROG, namely [5, 6, 7, 8, 9, 10, 11, 12, 13].

1.2 Outline

This dissertation is divided into five chapters: Introduction, Literature Review, Methodology, Results and Discussion, and Conclusion.

The first chapter introduced the work developed, its motivation and its objectives. The literature review chapter will summarize all the work developed by researchers on the topic under study. The chapter presents the starting point for the development of this work. In the third chapter, the methodology is presented. In this way, the whole experimental setup and proposed kinematics are described. The results obtained and their discussion will be presented in chapter four. In this way, the images referring to each of the study cases will be shown, as well as their analysis. Graphs of the flow separation as a function of the period fraction will be presented, and these will be analysed and discussed. The last chapter of this work will present the conclusions of this dissertation, adding perspectives for future work.

Chapter 2

Literature Review

This chapter presents the literature review, in which some of the work and research carried out by other authors is presented.

2.1 Biomimetics

Since the beginning of time, humankind has been looking for solutions to problems, such as the need for faster ways of locomotion and new materials that allow the production of stronger structures with applicability in several engineering areas. Finding these solutions has not always been easy and clear, but the answer could always be found in nature.

More recently, the term biomimetics has emerged as an exciting methodology that solves most of these problems. The term biomimetics originates from the Greek words *bios* (life) and *mimesis* (imitation), which means the imitation of nature [14, 15, 16]. However, biomimetics is not a recent study but an old idea of looking to nature for inspiration to solve problems. Biomimetics is used for various reasons, from knives inspired by the tooth structure of already extinct animals [17] to the composite materials we know today. Flying was a phenomenon inspired by birds and which emerged from their observation. On the other hand, fins used by divers are inspired by aquatic creatures such as seals.

The use of biomimetics in the aeronautical industry dates back many centuries, with the human desire to imitate the flight of birds and insects. In 1485, Leonardo da Vinci developed his first ”flying machine” (Figure 2.1), intending to imitate the flight of birds and bats. In some of his designs, the pilot was seated and in others, lying down, using his hands and feet to move the wings [18]. Leonardo’s observations, drawings and descriptions of the flight of birds were a significant advance in the study of aerodynamics [19].

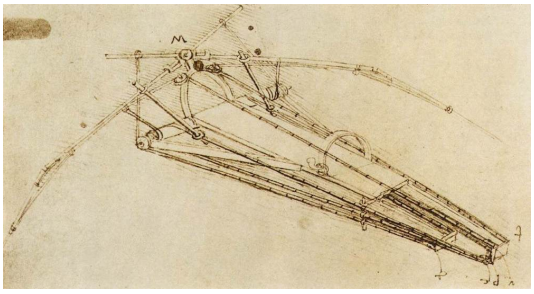

Figure 2.1: Leonardo da Vinci’s ”flying machine”.

At this time, it was thought that the resulting aerodynamic force could result from only the

wing, as happens in the flight of birds. Only later was realised that this resultant aerodynamic force would have to be divided into two components, lift and thrust. Thus, it was concluded that each of these forces should emerge from different places, as is the case today, where the engine produces the thrust force and the wing produces lift.

In 1903, the Wright brothers observed the eagle's wing, thus managing to build a powered aircraft (Figure 2.2), succeeding in its flight for the first time in human history [20]. Over the years, they have evolved this aircraft, making it faster, more stable and with a more aerodynamic shape, which means less drag.

Figure 2.2: First successful powered flight.

Today biomimetics can be found in many places and used in various fields of study, such as architecture, medicine and engineering.

In architecture, the most notable example is the buildings constructed based on termite nests. These nests exist in Africa and can reach up to $6\,\mathrm{m}$ in height. Since termites are extremely sensitive to heat, their nests maintain an ideal internal temperature for these animals. Through observing these nests, Mike Pearce built the Eastgate Centre (Figure 2.3), Zimbabwe's first all-natural cooling structure, in 1996. London Portcullis House (Figure 2.4), built in 2001, and Council House Two in Melbourne (Figure 2.5), built in 2006, are also buildings inspired by termite nests. These buildings have holes in the roof and floor, which allow natural ventilation, enabling warm air to escape through the roof and the inflow of cold air from below to ventilate the building. This is an alternative cooling system to artificial air-conditioning [21].

Figure 2.3: Eastgate Centre.

Figure 2.4: London Portcullis House.

Figure 2.5: Council House Two.

In the aviation industry, it is still necessary to look at nature to solve some of the problems we face [22, 23].

New materials are found through nature with better structural characteristics, allowing stronger structures with the same weight when compared with others already used. Honeycombs, built by bees in the dark, consist of perfect hexagonal structures. For bees, these structures provide stability using the least amount of material necessary. Thus, this is an ideal structure for constructing aircraft control surfaces and can be found in elevators, tails, wings and other components with large dimensions, needing strength while maintaining a low weight. Composite materials consist of a set of fibres held together by a matrix, often found in animals and plants. This combination of fibres and matrix gives structural and flexible properties combined with low weight. In this way, composite materials are widely used in various aircraft components.

Larger birds, like eagles, twist and flex their wings and feathers to maximise flight efficiency. These mechanisms were also adapted to aircrafts, for example, through flaps and winglets. Like the twist of birds' wings, flaps increase the wing area and its curvature, being possible to achieve higher lift. Birds turn their tip feathers upwards to reduce the effect of wing tip vortices, removing their energy. Winglets are the adaptation of this mechanism to aircrafts. This allows a reduction of wing tip vortices, increasing the aerodynamic efficiency.

Many robots have been built for terrestrial and space exploration. Most of them are based on existing animals and can fly, jump, walk and swim in order to complete a particular mission.

Recently, biomimetics has been used to develop nano and micro air vehicles (NAVs and MAVs). These vehicles can be defined as extremely small and lightweight systems [24]. In 1997, DARPA started a " MAV-project " programme, which presented the minimum requirements of these vehicles. It was defined that their dimensions should not exceed $15\,\mathrm{cm}$ in length, weighing less than $100\,\mathrm{g}$, with payload. These vehicles have mostly military applications, capable of performing indoor and outdoor missions in challenging environments and

performing intelligence, survival and reconnaissance missions. However, NAVs and MAVs have some challenges that must be overcome. Due to their small size, they have to keep all larger aircraft components in a small volume, significantly increasing their complexity. Another problem they face is the low Reynolds number environment in which they operate. Efforts have been made to understand flight at even lower Reynolds numbers by studying the flight of insects whose size is even smaller than that of a NAV [25, 26]. Thus, micro and nano air vehicles is an area of study that still needs a lot of research in order to overcome the problems and challenges still faced.

2.2 Flapping Motion

By observing the flight of birds and insects, it is observed that they produce thrust and lift through the flapping of their wings. However, it is difficult to replicate the natural motion of these animals' wings. Thus, the flapping motion is usually divided into three types of movement, as shown in Figure 2.6. In Figure 2.6a, there is the horizontal motion or surging, in Figure 2.6b, the vertical motion, or plunging, and finally, in Figure 2.6c, the rotational motion, or pitching.

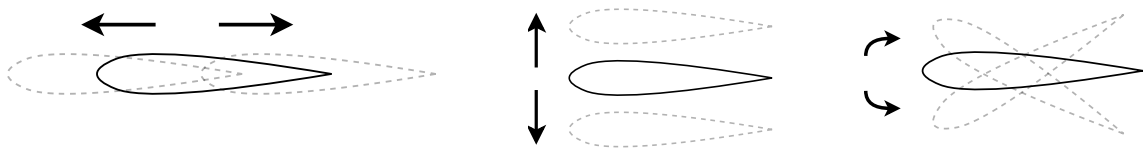

(a) Surging Motion. (b) Plunging Motion. (c) Pitching Motion.

Figure 2.6: Three types of motion in which the flapping motion is divided.

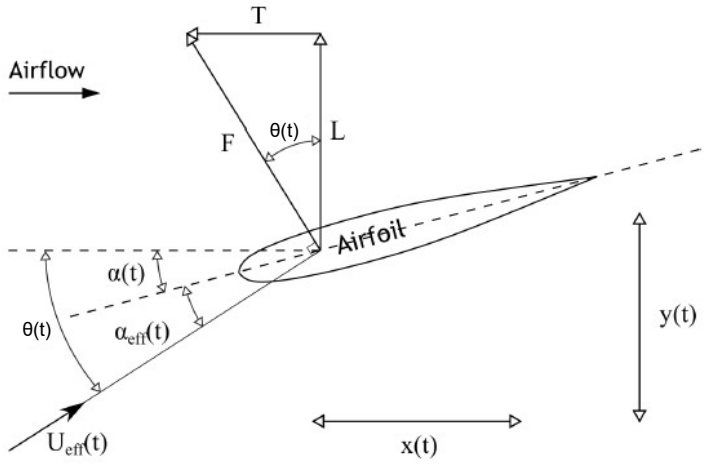

Figure 2.7: Schematic of foil kinematics [27].

These three motions form the flapping movement observed in Figure 2.7, where F represents the resultant aerodynamic force, being its components T, thrust, and L, lift. The angles $\alpha(t)$, $\alpha_{\text{eff}(t)}$ and $\theta(t)$ corresponds to angle of attack, effective angle of attack and pitch angle, respectively, while the motions $x(t)$ and $y(t)$ are the surging and plunging motions.

2.3 Governing Parameters

By observing the flight of birds and insects to replicate their movement, it is noted that they operate in diverse environments and conditions, adapting the movement of their wings to take these conditions into account. Reynolds number is an essential parameter since birds' flight strategies, which operate at relatively high Reynolds numbers, differ from those used by insects, which fly at extremely low Reynolds numbers.

In order to analyse the wings movement of flying animals, it is necessary to consider several dimensionless parameters needed to formulate the problem. In this way, these parameters can be divided into four types [28]:

1. Environmental parameters, which describe the fluid properties;
2. Geometric parameters, describing the shape of foils;
3. Kinematic parameters, describing the motion of foils;
4. Performance parameters, describing the propulsion and possible energy harvesting performance of foils.

2.3.1 Environmental Parameters

The environmental parameters describe the properties of the fluid in consideration. There are several fluid properties, but not all of them are used in the study of flapping airfoils. Reynolds number is one of these parameters and corresponds to the ratio between the inertial and the viscous forces, used to characterize the flow, being defined by 2.1.

$$\mathrm{Re} = \frac{\rho U_\infty c}{\mu}, \tag{2.1}$$

where ρ is the fluid density, U_∞ is the flow velocity, c is the airfoil chord and μ is the dynamic viscosity of the fluid. The parameters ρ, U_∞ and μ, on which the Reynolds number depends, are also environment parameters since they describe the fluid properties.

2.3.2 Geometric Parameters

The parameters that determine the shape of an airfoil are the chord length, c, the maximum thickness, t, the span length, b, the curvature, and the planform. However, as for this study we consider only a 2D airfoil, the geometric parameters are only the chord, maximum thickness and curvature.

2.3.3 Kinematics Parameters

The oscillatory motion of an airfoil depends on several parameters. One of these parameters is the Strouhal number, which is essential for characterizing oscillatory flows and important

in thrust generation [29]. Thus, the Strouhal number is defined by

$$\mathrm{St} = \frac{fW}{U_\infty}, \tag{2.2}$$

where f is the motion frequency and W is the wake length, in which $W = 2A$. The parameter A is the motion amplitude and is usually divided by the aerodynamic chord, obtaining its dimensionless form. The nondimensional amplitude is then expressed by equation 2.3.

$$h = \frac{A}{c} \tag{2.3}$$

The reduced frequency is another kinematic parameter used to study flapping airfoils. It is a dimensionless parameter of the oscillation frequency that relates the approaching velocity of the flow and the velocity at which the airfoil is moving, being defined by

$$k = \frac{2\pi f c}{U_\infty} \tag{2.4}$$

The effective angle of attack, α_{eff}, is defined as the angle between the foil and the vertical velocity [30] being expressed by

$$\alpha_{\text{eff}} = \arctan\left(\frac{-\dot{y}(t)}{U_\infty}\right) + \alpha(t), \tag{2.5}$$

where $\alpha(t)$ is the angle of attack typically, defined as in equation 2.6.

$$\alpha(t) = \alpha_0 + A_\alpha \sin(2\pi f_\alpha t + \phi), \tag{2.6}$$

where A_α is the pitching amplitude, f_α is the pitching frequency and ϕ is the phase angle between plunging and pitching.

Since this work considers only the plunging case ($\dot{\alpha}(t) = 0$) and taking into account the definitions of nondimensional amplitude and reduced frequency, the effective angle of attack for the symmetric sinusoidal motion case is given by

$$\alpha_{\text{eff}} = \arctan(-kh\sin(2\pi f t)) + \alpha_0, \tag{2.7}$$

being its maximum value given by equation 2.8.

$$\alpha_{\text{eff}_{\text{max}}} = \arctan(kh) + \alpha_0, \tag{2.8}$$

where α_0 is the mean angle of attack, which is zero for the case under study, where only plunging exists.

In this way, given the definitions of Strouhal number and reduced frequency (equations 2.2

and 2.4), it is shown that

$$kh = \pi \mathrm{St}, \tag{2.9}$$

which represents the maximum dimensionless plunging velocity. This parameter also gives the maximum effective angle of attack during airfoil movement, as it can be concluded through equation 2.8.

2.3.4 Performance Parameters

The parameters that describe the propulsive performance of an oscillating airfoil are the thrust coefficient, power coefficient and propulsive efficiency. The average thrust, $\overline{C_t}$, and power, $\overline{C_P}$ coefficients are expressed by equations 2.10 and 2.11 [31], as

$$\overline{C_t} = -\frac{1}{\Delta t}\int_t^{t+\Delta t} C_d dt \tag{2.10}$$

and

$$\overline{C_P} = -\frac{1}{\Delta t}\int_t^{t+\Delta t} \dot{y}C_l + \dot{\alpha}C_m dt, \tag{2.11}$$

respectively, where C_d, C_l and C_m are the drag coefficient, lift coefficient and moment coefficient, respectively.

Thus, the propulsive efficiency is defined as

$$\eta = \frac{\overline{C_t} U_\infty}{\overline{C_P}} \tag{2.12}$$

2.4 Flapping airfoils

The study of flapping wings began with the investigations of Knoller [32] and Betz [33] in 1909 and 1912, respectively. They were the firsts to observe that an oscillating wing creates an effective angle of attack. This effective angle of attack varies over time, creating an oscillatory aerodynamic force normal to the relative velocity [34]. The aerodynamic force created is decomposed into thrust and a lift [35], as portrayed in Figure 2.8. However, Knoller and Betz's theory is only based on the movement of the airfoil, not considering the vortex shedding, which was later proved to play a crucial role in identifying thrust production.

One of the first experimental validations of the Knoller-Betz effect was performed by Katzmayr in 1922 [36]. This experimental verification consisted in measuring the average thrust of a stationary airfoil placed in a sinusoidal oscillating wind flow [37]. In 1924, Birnbaum [38] studied various types of devices that use flapping motion, suggesting that the use of sinusoidal plunging wings could be an alternative to conventional propellers. Earlier studies by the author identified the conditions that lead to flutter or thrust generation [39].

In the following years, the aerodynamics of pitching and plunging airfoils received more at-

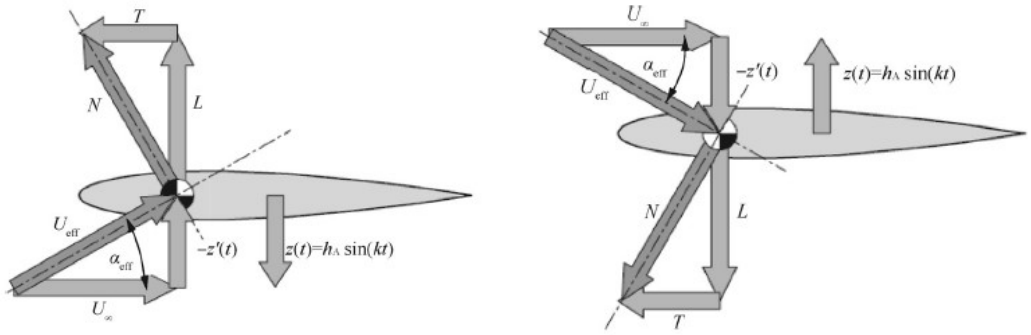

(a) Downstroke.

(b) Upstroke.

Figure 2.8: Knoller and Betz theory describing the propulsion of a flapping wing [35].

tention from researchers. However, it was only in 1935 that the first explanation of the production of drag or thrust is proposed by von Kármán and Burgers [40]. They theoretically explained the production of drag and lift by observing the shedding of vortices in the wake of an airfoil at low Reynolds numbers. The interaction of the flow with a bluff body, flat plates or airfoils in a pure plunging motion, pitching or combination of the two motions, produces significant differences in the visualized wake [41].

Kármán and Burgers observed that the wake generated by the interaction of the flow with a bluff body produces a set of vortices, commonly referred to as the von Kármán vortex street, observed in Figure 2.9. This type of wake vortex configuration causes a momentum deficit in the wake which produces drag.

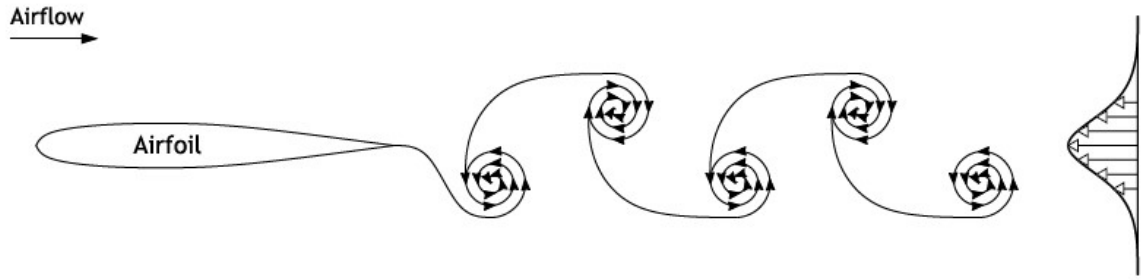

Figure 2.9: Typical von Kármán vortex street [42].

On the other hand, when the flow passes through a flat plate or an airfoil in a pure plunging motion, pure pitching or combination of the two, with a particular frequency, amplitude and/or velocity of oscillation, it may produce a wake where the vortices induce momentum, creating a jet-like flow. This type of wake is associated with the production of thrust, and the set of vortices formed is called an inverted von Kármán street, shown in Figure 2.10.

Freymuth [43] studied these concepts experimentally in 1988 by investigating the interaction of the flow with a NACA0015 airfoil in pure plunging and pure pitching motion. In this way, von Kármán vortex streets were observed for both airfoil motions. It has been demonstrated that a rigid airfoil in pure pitching or pure plunging motion can produce thrust. The results

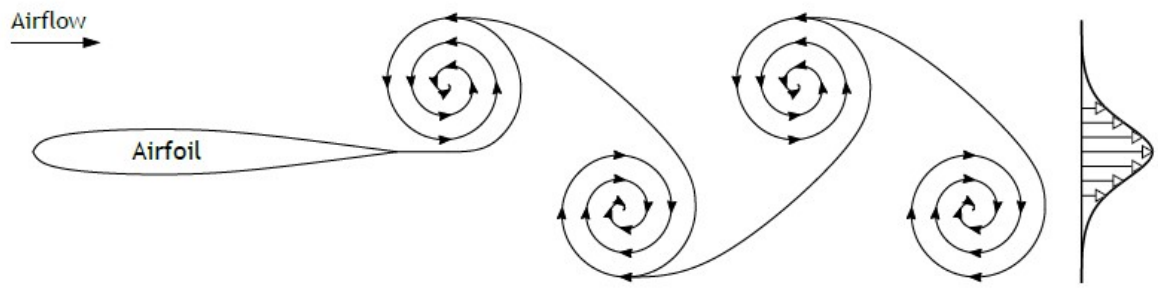

Figure 2.10: Inverted von Kármán vortex street [42].

showed that an increase in pitching or plunging amplitude causes a flow separation on the airfoil's leading edge. A decrease in reduced frequency results in an increase in the distance between the vortices.

Jones et al. [44] used a laser Doppler velocimetry to obtain high-resolution velocity measurements in the wake of pure plunging airfoils in a water tunnel. Their results agreed with the calculations of Triantafyllou et al. [45], who identified the Strouhal number as an important parameter in the generation of thrust, once the optimal efficiency is achieved for Strouhal number between 0.25 and 0.35.

In 1936, Garrick [46] applied the theory of Theodorsen [47] to determine the thrust produced by an airfoil in a low-amplitude plunging motion in an inviscid and incompressible fluid. He concluded that the pure plunging motions generate thrust and that thrust is proportional to the square of the motion frequency [48]. Lighthill [49] also calculated the thrust force and efficiency for an inviscid model [50].

Lai and Platzer [51] and Young [52] studied the formation and stability of various vortex wake configurations. They observed drag producing wakes and thrust producing wakes, also appearing wakes that represent the transition from the drag production wake to the thrust production wake, illustrated in Figure 2.11. Young and Lai [53] found that this type of wake is created due to the interaction between the bluff body natural shedding (momentum deficit that produced drag) and the motion of the airfoil (induced velocity or momentum). This interaction causes a transition from a typical von Kármán vortex street and to inverted von Kármán vortex street.

In 1953, by studying the wake of a NACA0015 airfoil in oscillatory motion, Bratt [54] discovered a new type of wake. When an airfoil is subjected to high reduced frequencies and plunging amplitudes, i.e. high Strouhal numbers, the appearance of a deflected vortex street occurs, seen in Figure 2.12. It was only in 2004 that this type of wake was studied in more detail by Jones et al. [55]. The effect of plunging frequency and amplitude on the characteristics of the wake of an airfoil was investigated. The flow solutions were computed using an unsteady, flow-potential code developed by Teng [56] with a visualization software developed by by Jones and Center [57]. He concluded that for values of Strouhal number greater

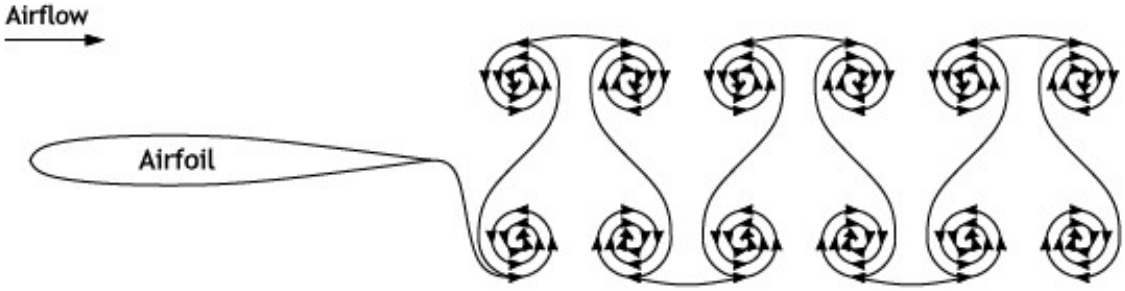

Figure 2.11: Transition from typical to inverted von Kármán vortex street [42].

than 1, deflected wake patterns were found experimentally and numerically. Numerically, the direction of the deflection (deflected upwards or downwards) seems to be determined by the initial conditions. However, experimentally, alternation in wake deflection was observed, suggesting that small perturbations may be sufficient to alter wake deflection.

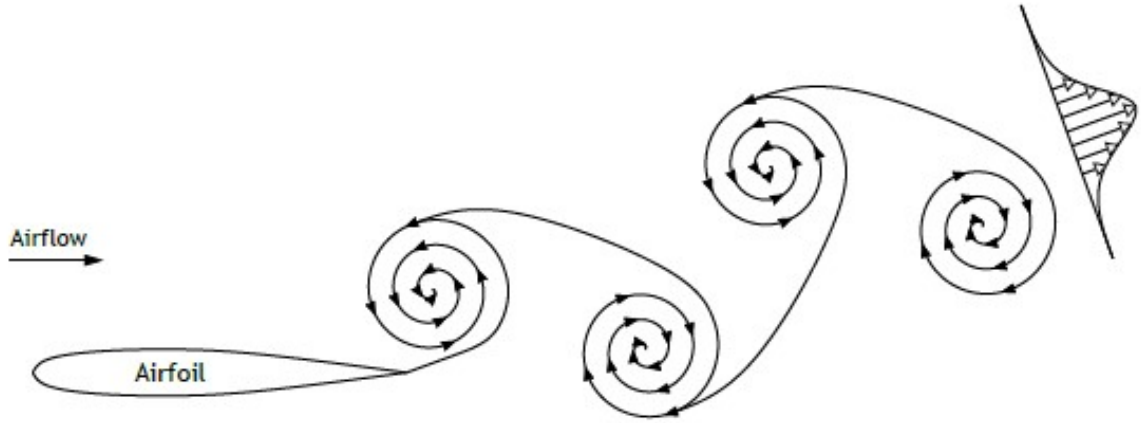

Figure 2.12: Deflected vortex street [42].

Using a Navier-Stokes code, Tuncer and Platzer [58], in 1996, studied the thrust and propulsive efficiency of a flow passing through an airfoil in pure plunging motion. It was found that a flapping airfoil generates thrust and a propulsive vorticity pattern that is quite different to the typical drag-producing vorticity pattern generated by a stationary cylinder. It was verified that the cylinder produces a vortex street where the top vortices rotate clockwise and the bottom, anticlockwise. In contrast, anticlockwise rotating vortices are located at the top in the wake of thrust producing of a flapping airfoil. These two authors also studied the flow over a combination of flapping/stationary airfoils in a tandem configuration. It was concluded that a stationary airfoil in the wake of a flapping airfoil significantly enhances the total thrust and propulsive efficiency.

Tuncer et al. [59] visualized and measured the wake characteristics of a NACA0012 airfoil in pure plunging motion and combined plunging/pitching motion. It was observed that by varying the frequency and amplitude of the pure plunging oscillatory motion, the appearance of stall occurs as soon as the value of the dimensionless plunge velocity kh exceeds the value of 0.35. However, they found that further studies would be necessary to explore the stall's

nature.

In 1999, Isogai et al. [60] used a Navier-Stokes code to clarify the effects of the dynamic stall phenomenon on the propulsive efficiency and thrust of an airfoil in oscillatory motion. The motion under consideration is a combination of pitching and plunging motions for various combinations of reduced frequency, amplitudes and phase angle between the two motions. It was concluded that the phase angle between the plunging and pitching motions is a critical parameter affecting the propulsive efficiency. Two years later, Ramamurti and Sandberg [61] also used a Navier-Stokes code to compute the flow interaction with a NACA0012 airfoil in combined pitching and plunging motion. The phase angle between the movements was varied. After the analysis of the results, there was an agreement with the experimental results of Anderson [62], which showed that optimum propulsive efficiencies were obtained within an approximate range of Strouhal numbers of 0.2-0.4. This range of Strouhal numbers for optimal propulsive efficiency was also confirmed by Taylor et al. [63] through the study of flying animals in cruise flight, being also observed in fish and dolphins. Taking into account the variation in the lift coefficient, it is observed that a slight decrease in lift during the cycle is due to the attachment of a vortex on the airfoil's upper surface. Once this vortex is released, the value of the lift coefficient starts to increase again.

In 2004, Young and Lai [64] studied the details of wake structure, lift and thrust generation, and their dependence on plunging frequency and amplitude for an airfoil in a pure sinusoidal plunging motion. The simulated airfoil is a NACA0012 airfoil that is put through a Navier-Stokes solver, assuming laminar and turbulent flows. The comparison between the simulations in fully laminar and fully turbulent flow showed significant differences due to the flow's behaviour at the airfoil's trailing-edge. However, it was observed that the aerodynamic forces only differ when the separation at the leading-edge is evident. These results indicate that, for these Reynolds numbers, leading-edge effects are essential in determining the forces resulting from the motion of the plunging airfoil. On the other hand, trailing-edge effects significantly influence the wake structures but only have a secondary influence on the production of lift and thrust. Later, these authors also studied the effect of flow separation on the thrust production and the efficiency of an airfoil in sinusoidal pitching and plunging motion [65]. Flow separation and vortex shedding at the leading edge are predicted to depend on the reduced frequency. Thus, the propulsive efficiency peaks for a Strouhal number between 0.1 and 0.4. The magnitude and the Strouhal number to which this maximum value corresponds, depends on the type of motion considered.

More recently, in 2016, Geissler and van der Wall [66] investigated the flow around an airfoil in a plunging motion. It was considered the dynamic deformation of the NACA0012 airfoil, through leading-edge deformation, to analyse its influence on the flow structures. Generation of thrust and propulsive efficiency were investigated for the deformed and nondeformed airfoil configuration. It was concluded, through results, that the deformed airfoil can produce higher thrust, but the power coefficient is smaller when compared with the rigid airfoil. Relatively to propulsive efficiency, it is shown that the deforming airfoil achieves higher values.

In 2017, Yu et al. [67] simulated the impact of an approaching shear flow on vortex structures around a flapping NACA0012 airfoil using a Navier-Stokes flow solver. The results obtained from the simulations found that shear flow promotes the formation of dipole vortices in the wake of the airfoil, which can contribute significantly to the production of lift. The lift produced through shear flow was compared with that obtained by increasing the airfoil's angle of attack in a uniform flow. It was concluded that when generating the same amount of lift, the airfoil in shear flow can generate more thrust than the one with a larger angle of attack. This indicates that flapping wing design can benefit from shear flows as it can produce higher lift without compromising the thrust generation.

Luo et al. [68] performed a numerical study of the aerodynamic performance of a plunging NACA0014 airfoil for a Reynolds number of 10^4. The aerodynamic forces and wake structures were analysed. The results indicate that increasing the amplitude or frequency of plunging increase the lift force in forward flight. A decrease in plunging amplitude or frequency will result in a lower produced lift force and thrust force.

Over the years, the aerodynamics of pitching and plunging airfoils have received much attention from researchers. Most of the studies involve sinusoidal pitching and/or plunging motions and consider propulsive performance and flow structure analysis.

2.5 Studies of flapping wings under asymmetric kinematics

Some work has also been carried out to learn more about asymmetric conditions of pitching and plunging airfoils.

In 1989, Koochesfahani [69] studied the vorticity patterns in the wake of a NACA0012 airfoil in asymmetric pitching motion at low amplitudes. This study was carried out in a low-speed water tunnel. The effect of the asymmetric oscillation is demonstrated through the parameter S, which is the percentage of the period required to reach the maximum amplitude from the minimum amplitude. It was observed that the wake structure of a pitching airfoil could be substantially modified by changing the amplitude, frequency and shape of the oscillation waveform, through the change on S parameter. In this experiment, the airfoil produced thrust at a higher reduced frequency than indicated by calculations based on classical linear inviscid theory, since it takes into account the presence of viscous drag. In addition, the value of the critical reduced frequency for thrust generation appears to depend on the oscillation amplitude.

Xiao and Liao [70] numerically investigated the effect of asymmetric oscillatory motion on the propulsive performance of a pitching airfoil to verify whether the thrust produced by pure pitching motion can be improved by asymmetric oscillation. The tests were performed for different frequencies, pitching amplitudes, and asymmetry level. It was concluded that for symmetrical and asymmetrical sinusoidal pitching, the thrust coefficient and power coefficient increase with oscillation frequency for a given pitching amplitude. However, the

propulsive efficiency remains relatively constant. Higher pitching amplitude results in the generation of higher thrust but has less effect on efficiency. It was verified a significant improvement in thrust coefficient for the asymmetric case. By observation of wake structures, it is concluded that a stronger Kármán vortex street is notable for higher levels of asymmetry compared with the symmetric case. After analysing the computational obtained results, these two authors suggested that the asymmetric sinusoidal motion could be a better tool for thrust performance for pure pitching motion.

Lu et al. [71] evaluated the effects of high amplitude, asymmetric pitching motion and camber on the propulsive performance of a pitching airfoil. These effects were studied numerically, and a NACA0012 airfoil was used to investigate the influence of large amplitude and asymmetric pitching motion. For the impact of camber, several 4-digit NACA airfoils were used. The results showed that the thrust and power coefficients increase with reduced frequency for a fixed value of pitching amplitude for both symmetric and asymmetric pitching motion. However, the propulsive efficiency decreases with pitching amplitude when keeping the reduced frequency constant. Observing the airfoil wake, an inverse von Kármán vortex street is verified for higher values of reduced frequency. Larger pitching amplitudes lead to bigger thrust generation, but this parameter has little effect on propulsive efficiency. For larger asymmetry levels, it is observed a stronger von Kármán street. This is believed to be the reason why an increase in asymmetry level leads to thrust production. The study of the effect of camber revealed that varying the camber or its location offers no benefit in thrust generation and propulsive efficiency when compared to symmetric airfoil sections.

Lu et al. [72] studied, in 2013, the effect of asymmetric sinusoidal pitching motion on the force coefficients of a NACA0012 airfoil. They also investigated how asymmetric motion affects the flow around the airfoil. The asymmetric sinusoidal motion was tested numerically for pitching motion, and the obtained results conclude that the the asymmetry parameter has a great impact in flow structures and vortex development, since an increasing in asymmetry level, leads edge vortices to form later, resulting in less drag coefficient.

A numerical investigation was carried out by Zhang et al. [73] to evaluate the effect of asymmetric oscillatory motion on the aerodynamic performance of a plunging NACA0012 airfoil. Conventional and asymmetric sinusoidal movements were studied for plunging oscillations and their impact on thrust and propulsive efficiency. From this experiment, it was concluded that more thrust can be generated through the asymmetric sinusoidal motion compared to the sinusoidal case. Furthermore, it was found that the greater the asymmetry, the more thrust is generated and higher the propulsive efficiency. Significant differences in wake patterns are observed for different values of the asymmetry parameter. For the symmetric case, $(S = 0.5)$, multiple vortices are formed during the motion cycle, being formed in the upstroke and downstroke with the same strength. For the level of asymmetry with a faster downstroke motion $(S = 0.25)$, one strong vortex is formed during this phase. On the other hand, for $S = 0.75$, a strong vortex is formed on the upstroke phase of the motion.

In order to study asymmetric motion on pitching airfoils and improve the energy extraction, Teng et al. [74] performed a numerical simulation, considering a NACA0015 airfoil with a Reynolds number of $\mathrm{Re} = 1 \times 10^3$. The motion is a trapezoidal-like pitching profile. However, no relevant conclusions were drawn regarding energy extraction due to the asymmetric motion of the airfoil, since they tried to increase the power generation to the optimal values of pitching amplitude and frequency, finding that the energy harvesting values decreased. Thus, it was concluded that the efficiency improvement strategy by using trapezoidal-like pitching profiles is ineffective when optimal parameters are considered. This topic stays open for further investigation.

Sankarasubramanian et al. [75] combined the study of airfoil thickness with asymmetric motion with three objectives. The first objective was to study the effect of airfoil thickness on thrust generation for various reduced frequencies and nondimensional plunge amplitudes. For this study, four airfoils were considered, NACA0012, NACA0015, NACA0018 and NACA0030. The second objective was to study the effect of asymmetric plunging motion on thrust generation, for various values of reduced frequency and nondimensional plunge amplitude. Finally, the third and last objective was to study the propulsive efficiency of various airfoils and plunging motion. After analysing the results, it was concluded that the airfoil thickness is directly related to the generation of LEVs and TEVs, influencing the propulsive efficiency of airfoils at low Reynolds numbers. The formation of LEVs has a significant role in thrust generation and the vortex strength increases with the Strouhal number. It was also concluded that the propulsive efficiency is higher for symmetric motion, but less thrust is generated when compared to the asymmetric case.

Asymmetric motion conditions were also experimentally studied by Rodrigues et al. [42], who analysed the wake structures created due to unequal ascending and descending velocities in plunging motion, using a NACA0012 airfoil. The results showed that when asymmetry is used, the airfoil can produce thrust and lift simultaneously. It was possible to visualize the formation of LEVs on the airfoil's upper surface, which could be indicative of power extraction mechanisms since a low-pressure zone during the ascent phase helps reducing power.

Pure plunging under asymmetric conditions was studied numerically by Torres et al. [76], where a brief comparison with experimental data was performed. This work aimed to predict the flow around an oscillatory NACA0012 airfoil through simulations in CFD and LESP-modulated discrete-vortex method (LDVM), proposed by Ramesh et al. [77]. The results indicated that the reduced-order method gives good results, reinforcing the already known conclusions that inviscid phenomena governs wake vortices and their convection.

In 2021 Mekadem et al. [78] studied the influence of asymmetric motion on flapping airfoils, including pitching and plunging motions, using a NACA0014 airfoil. A numerical parametric study was performed to evaluate the effect of kinematic parameters such as the oscillation frequency, pitch and plunge amplitudes, and the phase angle between pitch and plunge on thrust and propulsive efficiency of an oscillating airfoil at low Reynolds numbers. After

analysing the obtained results, it was concluded that the best propulsive efficiency is obtained for a sinusoidal flapping trajectory, Strouhal number of $\mathrm{St} = 0.2$, phase angle of $\phi = 90^\circ$ and pitch angle between 15° and 25°. It was also concluded that the best thrust is achieved for nonsinusoidal flapping trajectory, Strouhal numbers between 0.2 and 0.35, and phase angle of $\phi = 100^\circ$.

As presented above, several researchers have studied asymmetric movement with regard to flapping foils. However, it can be seen that this area still needs much research and evolution. The most studied topics are asymmetric motion in computational analysis of airfoils in pure pitching motion. Regarding the experimental study of the asymmetric motion of airfoils in pure plunging motion, there is almost no work done. Thus, this work allows the study of this motion in a detailed way. An experimental study of a NACA0012 airfoil in plunging motion is carried out, comparing the symmetric and asymmetric motion. The main objective of the work will be to study the influence of the motion asymmetry level, the nondimensional amplitude and the reduced frequency on the wake patterns of this airfoil. This is a topic with much potential since it proposes the variation of the aerodynamic force resulting from the wing motion, only through the motion kinematics, instead of making changes in the airfoil geometry.

Chapter 3

Methodology

This third chapter is divided into three parts, the experimental setup, motion kinematics, and experimental validation. All materials and equipment used to perform the experiments are presented and explained in the experimental setup. In the motion kinematics subsection, the movement prescribed to the airfoil will be examined. Finally, an experimental validation is performed to verify if the motor follows the desired motion.

3.1 Experimental Setup

The experimental setup is based on the installation projected in [79, 80]. This installation consists of a wind tunnel, a smoke generator, a led light panel, an anemometer, a wing with the NACA0012 airfoil, an electric motor, a linear actuator, a controller, a computer, and a high-speed camera. Figure 3.1, shows a simplified installation scheme. Experiments are conducted at the Aeronautics and Astronautics Research Center (AEROG).

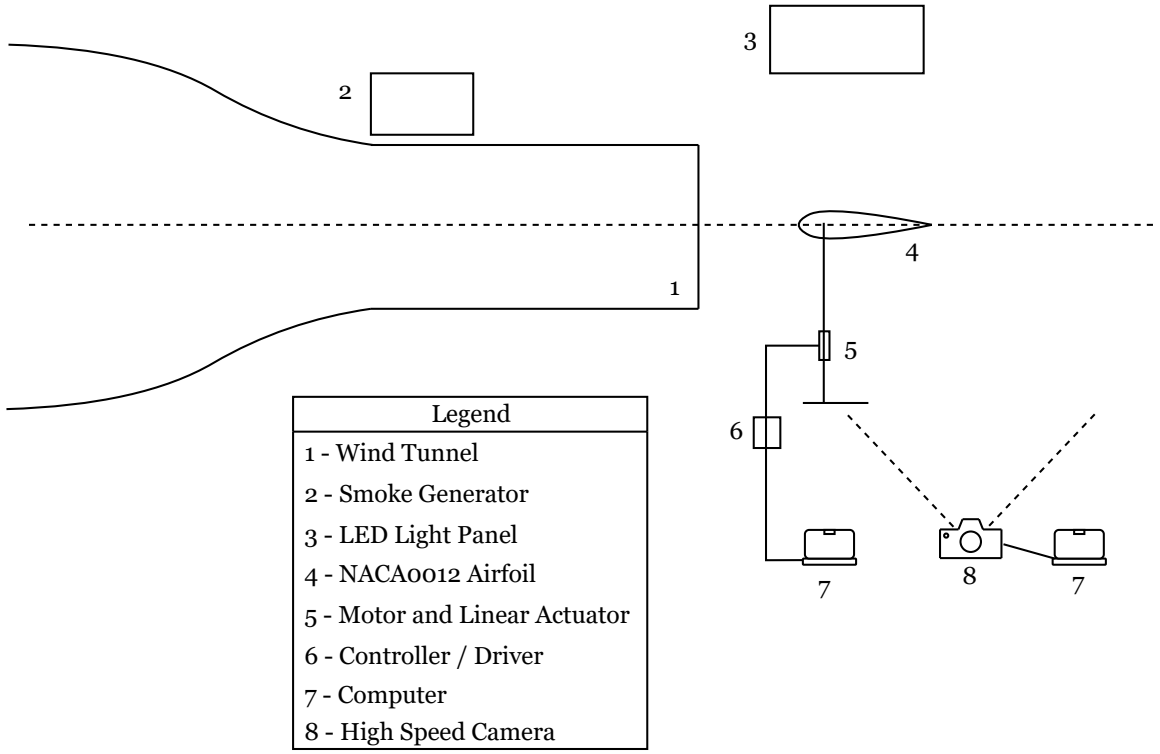

Figure 3.1: Experimental setup, adapted from [42].

The wing is attached to a metal structure linked to a linear actuator and placed approximately $0.02\,\mathrm{m}$ from the tunnel exit. The linear actuator performs its movement through the connec-

tion to a stepper motor. Flow visualization is achieved using a smoke machine, being the smoke particles illuminated by a LED panel. The flow is captured using a high-speed camera. Next, each element of the experimental setup will be presented, as well as an explanation of its function.

3.1.1 Wind Tunnel

The wind tunnel used for the experimental tests (Figure 3.2) is a subsonic tunnel developed in 2004 at Aeronautics and Astronautics Research Center, Universidade da Beira Interior [81]. This is an open-section wind tunnel, where the exit section is $0.2\,\mathrm{m}$ by $0.3\,\mathrm{m}$. The air speed at the tunnel's exit can be controlled in two ways. One is by opening and closing a guillotine that controls the amount of air entering the tunnel, with a maximum opening of $130\,\mathrm{mm}$. The other is through the modification of the motor's frequency.

Figure 3.2: Wind Tunnel.

3.1.2 Wing and Supports

The wing has the NACA0012 airfoil with a wingspan of $0.3\,\mathrm{m}$ and an aerodynamic chord of $0.2\,\mathrm{m}$, being built through 3D printing, using the Prusa i3 MK3S + 3D printer with PLA filament.

The wing is composed of two $8\,\mathrm{mm}$ diameter aluminium spars, ensuring the connection to the linear actuator structure. One of the spars is located at the maximum thickness of the airfoil, that is, at $60\,\mathrm{mm}$ from the leading-edge (30% of the chord) and the other at $110\,\mathrm{mm}$ from the leading edge. Taking into account the size limitations of the 3D printer, it was necessary to print the wing in three parts, being these attached through four pins, with a diameter of $6\,\mathrm{mm}$. Figure 3.3 shows three views of the projected wing as well as some main measurements, while Figure 3.4 shows a drawing of the wing's final assembly.

After the wing construction, it was sanded with the aim of obtaining a better surface quality, obtaining at the final result, seen in Figure 3.5.

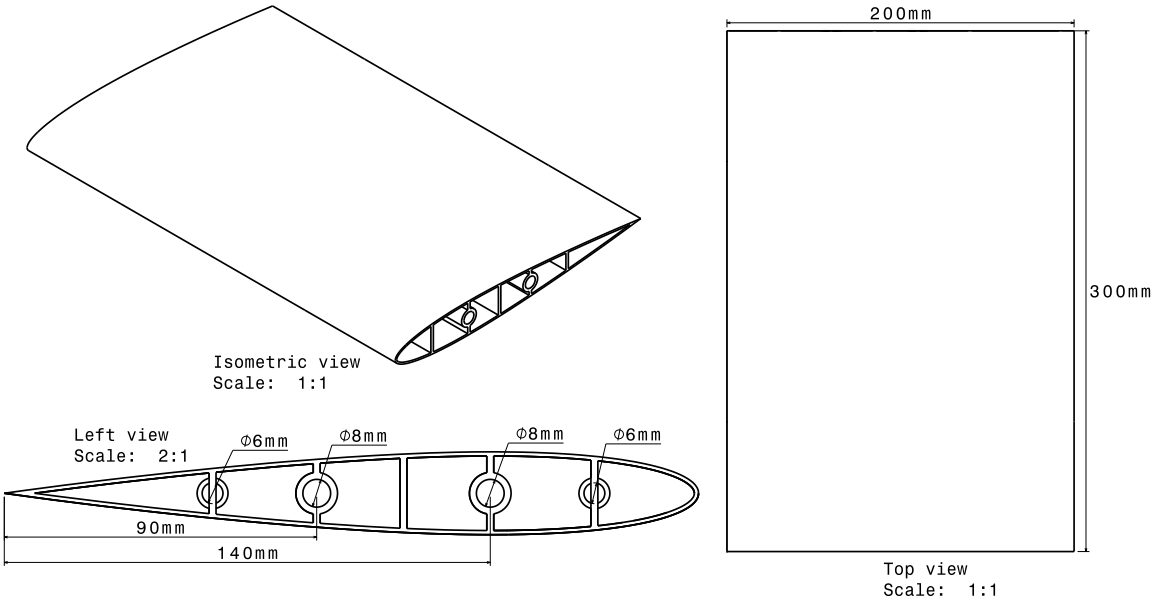

Figure 3.3: Isometric, top and left views of the projected wing.

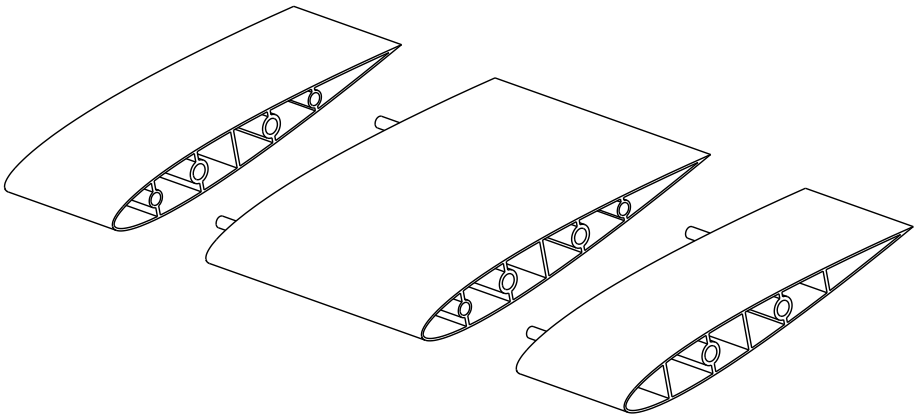

Figure 3.4: Final wing assembly.

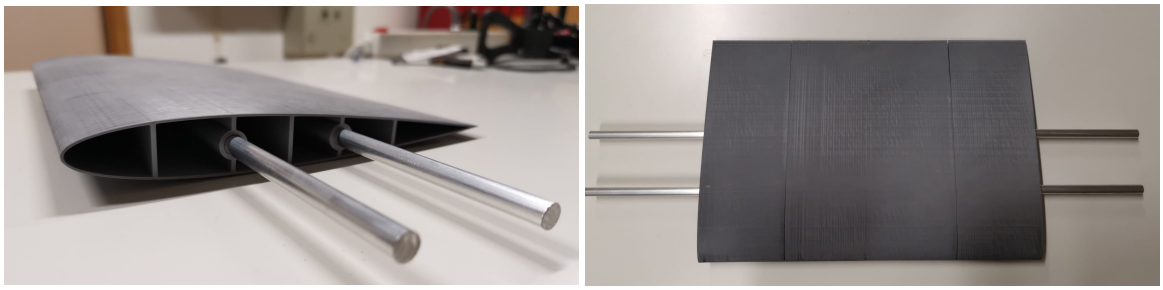

(a) Isometric view. (b) Top view.

Figure 3.5: Final Wing.

The linear actuator is connected to a metallic structure that allows its linkage to the wing. In this way, two supports were constructed to connect the metal structure to the wing spars.

These supports are 3D printed with PLA filament and allow the connection between the wing and linear actuator, being connected to the wing through its spars. The supports were designed to interfere as little as possible with the flow visualization, having the structure shown in Figure 3.6. Figure 3.7 shows the final support's configuration.

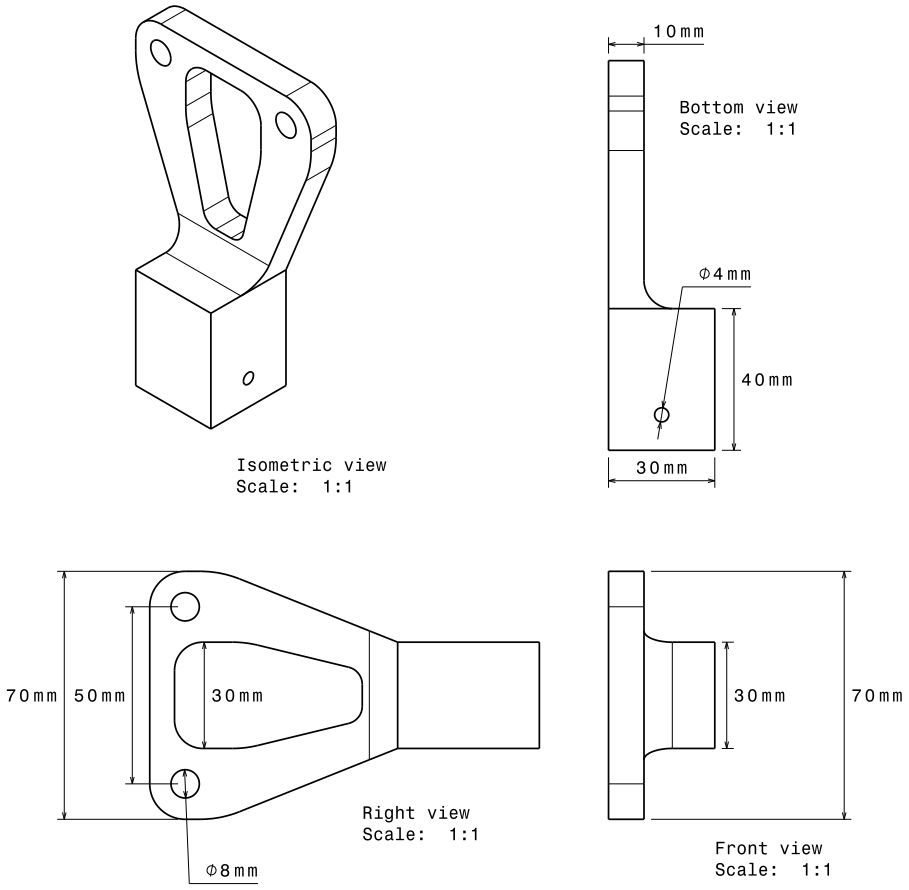

Figure 3.6: Isometric, bottom, right and front views of the supports connecting the wing to the linear actuator.

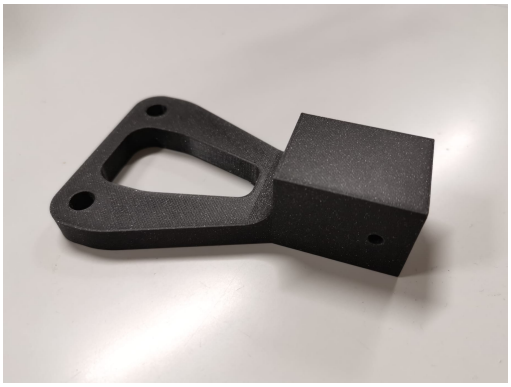

Figure 3.7: Final support.

After building both wing and supports, it was then possible to assemble the whole structure,

seen in Figure 3.8.

Figure 3.8: Wing, supports and linear actuator.

3.1.3 Smoke Generator

In order to observe the wake structures, a smoke system was used, presented in Figure 3.9. This Technofog smoke machine from the JEM manufacturer is composed of a smoke generator and a smoke controller. It has a 750W heating capacity and a heating time of 7min, having a tank with 1 L capacity. The smoke controller regulates the intensity at which the smoke is released from the generator and the frequency at which it occurs. In this study, the TIMER switch has been set to zero, and the FOG switch has been activated manually to allow the smoke release. On the other hand, the LEVEL switch, relating to the amount of smoke released, has been set for each case.

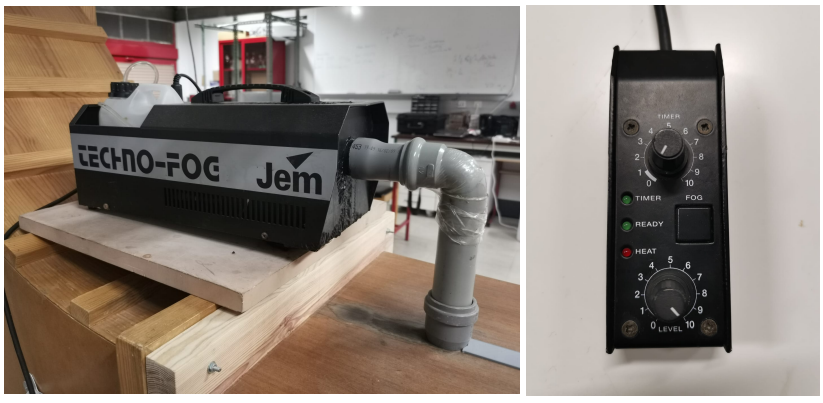

(a) Smoke Generator. (b) Smoke controller.

Figure 3.9: Smoke system.

3.1.4 Anemometer

Taking into account the ambient conditions, namely pressure and temperature, it was necessary to change the flow velocity at the exit of the wind tunnel to keep the Reynolds number

constant. This was possible using an anemometer as observed in Figure 3.10, to measure the flow's velocity at the wind tunnel's exit, making it possible to control this velocity even if the environmental conditions change. The anemometer is the Airflow TA410, which measures velocity with a straight, telescopic probe. As explained previously, the airspeed at the tunnel's exit can be changed by opening and closing a guillotine. Thus, the anemometer is placed outside the tunnel, and the guillotine is adjusted until the desired flow velocity is achieved.

Figure 3.10: Anemometer.

3.1.5 Motor and Linear Actuator

The motor used in the experimental tests, Figure 3.11a, is a motor from *Oriental Motors*, *AR series FLEX AC power input built-in controller type*, model *ARM46AC*, with a $0.36\,°/\mathrm{step}$. This motor is coupled to a linear actuator, Figure 3.11b with a step of $0.012\,\mathrm{mm}$, also from *Oriental Motors*, model *EASM4XD020ARAC*. The linear actuator has a maximum speed of $800\,\mathrm{mm\,s^{-1}}$ and a maximum thrust force of $100\,\mathrm{N}$.

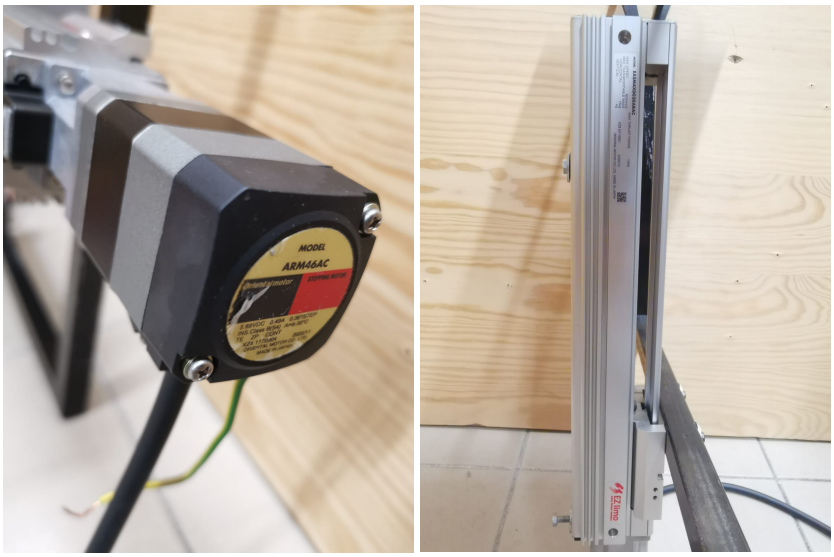

(a) Motor *ARM46AC*.

(b) Linear Actuator *EASM4XD020ARAC*.

Figure 3.11: Motor and linear actuator used in the experimental tests.

For the desired motion execution, the information is programmed in the MEXE02 software version 3.71, Figure 3.12, being subsequently stored in a controller. This controller is connected to the motor, where it will transfer the stored instructions, allowing the motion of the wing.

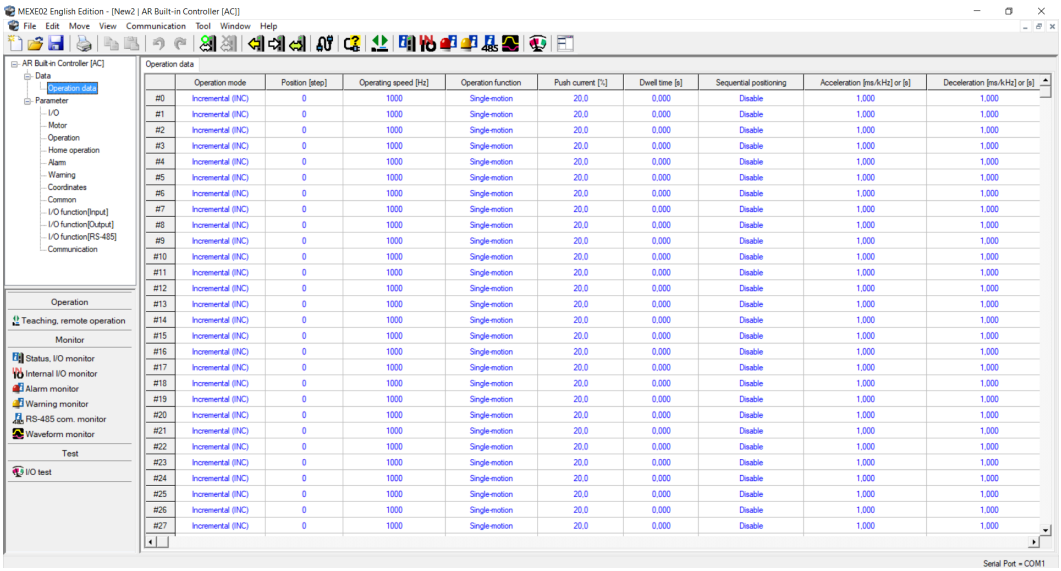

Figure 3.12: MEXE software.

3.1.6 Controller

In order to transfer the necessary movement from the software to the motor, an ARD-CD controller, Figure 3.13 from Oriental Motors was used. This controller is connected to a computer with the MEXE02 software, through a CC05IF-USB communication cable. The controller will store the information contained in the software. When necessary, a switch will be pressed, allowing the controller to transfer the data to the motor, thus enabling it to carry out the desired motion.

Figure 3.13: Controller.

3.1.7 High Speed Camera

To visualize the wake flow of the NACA0012 airfoil, it was used a high-speed camera, a *Photron FASTCAM MINI*, model *UX50*, Figure 3.14. This camera model provides an image resolution of 1280 x 1024 pixels with a frame rate of up to 2000 fps. The lens used is a

Canon EF-S 18-55mm f/3.5-5.6 IS II, a high-quality, standard zoom lens. The camera was placed at $90°$ from the plane of the airfoil and with a pitch-down angle of approximately $8°$ to observe the upper surface of the airfoil better. The images were saved with an image resolution of 1280 x 1024 pixels and a frame rate of 500 fps, using the Photron FASTCAM Viewer, being further processed and improved using MATLAB.

Figure 3.14: High Speed Camera.

3.2 Motion Kinematics

In this study, the NACA0012 airfoil is studied with plunging motion that follows a sinusoidal waveform. In this way, the motion can be described by

$$y = A\cos(2\pi ft), \tag{3.1}$$

being the plunging velocity given by

$$\dot{y} = -2\pi fA\sin(2\pi ft), \tag{3.2}$$

where y is the vertical position, and A and f are the amplitude and frequency of the motion, respectively.

Since the primary purpose of this work is to compare symmetrical and asymmetrical sinusoidal waveform plunging motions, a parameter was considered that allows the introduction of a level of asymmetry to the kinematics. This parameter is represented by the Greek letter ζ and is defined as the period percentage corresponding to the ascending phase. This means that $\zeta = 0.5$ corresponds to the conventional sinusoidal waveform. On the other hand, if $\zeta > 0.5$, the ascending motion is slower than the descending, meaning that the ascending phase occurs in ζT seconds. Thus, this parameter is defined by

$$\zeta = \frac{t_u}{T}, \tag{3.3}$$

where t_u represents the time of the upward motion and T corresponds to the motion period. Thus, t_d represents the time of the downward motion and is given by $t_d = T - t_u$.

Hence, the modified equations that govern the asymmetric sinusoidal kinematics are given

by

$$\begin{cases} y(t) = A\sin\left(\dfrac{2\pi}{2\zeta T}t + \dfrac{\pi}{2}\right) & \text{if } 0 \leq t < \zeta T \\ \\ y(t) = A\sin\left(\dfrac{2\pi}{2(1-\zeta)T}(T-t) + \dfrac{\pi}{2}\right) & \text{if } \zeta T \leq t \leq T \end{cases} \tag{3.4}$$

In Figure 3.15, the graph of equation 3.4 is shown. Using the equations of motion defined in

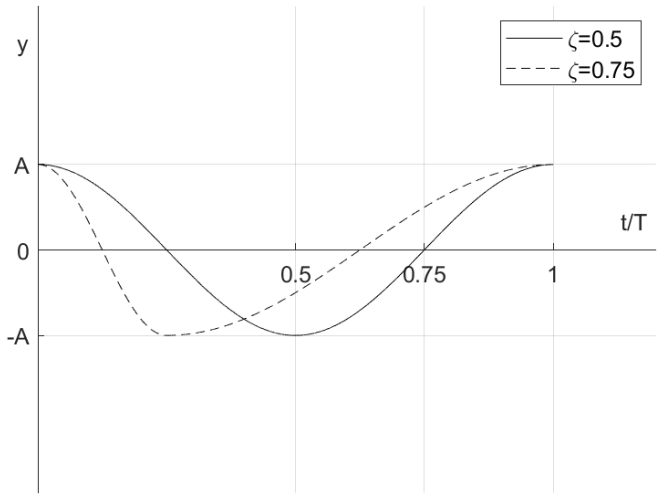

Figure 3.15: Airfoil kinematics.

3.4, it is possible to obtain the equations of effective angle of attack for this type of motion, through equation 2.5, defined in the Literature Review section, Chapter 2. Thus, the effective angle of attack is given by

$$\begin{cases} \alpha_{\text{eff}} = \arctan\left(\frac{-kh}{2(1-\zeta)}\cos\left(\frac{\pi}{(1-\zeta)T}t + \frac{\pi}{2}\right)\right) & \text{if } 0 \leq \frac{t}{T} < 1-\zeta \\ \\ \alpha_{\text{eff}} = \arctan\left(\frac{-kh}{2\zeta}\cos\left(\frac{\pi}{\zeta}\frac{t}{T} - \frac{\pi}{\zeta} + \frac{\pi}{2}\right)\right) & \text{if } 1-\zeta \leq \frac{t}{T} \leq 1 \end{cases}, \tag{3.5}$$

Since the motor software (MEXE02) can only perform trapezoidal movements, it was necessary to approximate this movement to a sinusoidal function. This process was performed using the acceleration parameter, ξ, which is a correction factor that approximates the periodic trapezoidal function to the sinusoidal function. The value of ξ was obtained through the upward (OS_u) and downward (OS_d) velocities, defined as

$$OS_u = \frac{2A}{\zeta T(1-\xi)} \tag{3.6}$$

$$OS_d = \frac{2A}{(1-\zeta)T(1-\xi)} \tag{3.7}$$

The velocity of the wing is conditioned by the maximum velocity the motor can reach. The downward velocity is the critical one since this is always equal or higher than the upward speed. The motor speed limit is $OS = 0.8\,\mathrm{m\,s^{-1}}$, which corresponds to $OS = 66\,667\,\mathrm{step/s}$,

which means that for each condition tested, the descent speed can never exceed this value.

Thus, it was possible to obtain the value of the acceleration parameter iteratively, obtaining the following result

$$\xi \simeq 0.32881 \tag{3.8}$$

In Figures 3.16 and 3.17, a representation of the position and velocity graphs with the *sine* function approximation is observed, being presented both symmetric and asymmetric ($\zeta = 0.75$) conditions.

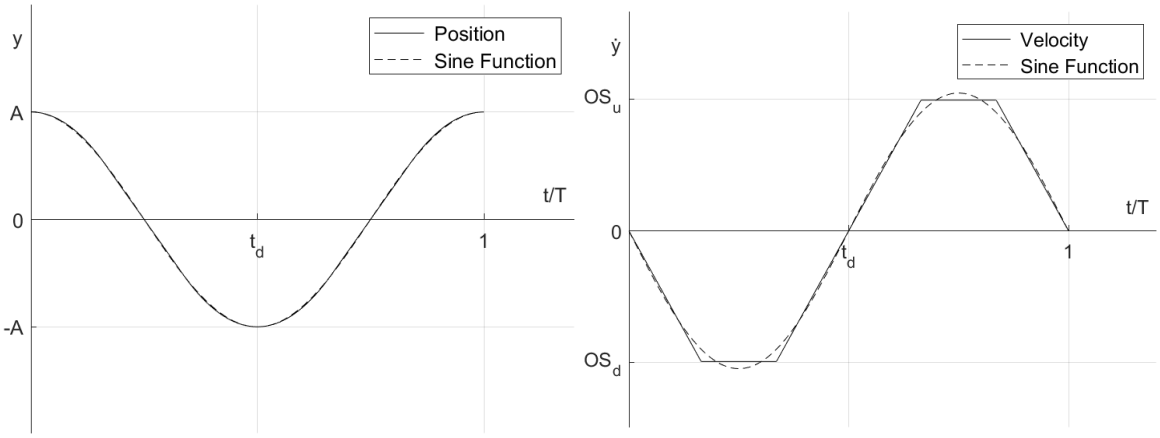

(a) Position as a function of period fraction for a symmetric motion.

(b) Velocity as a function of period fraction for a symmetric motion.

Figure 3.16: Symmetrical motion profile.

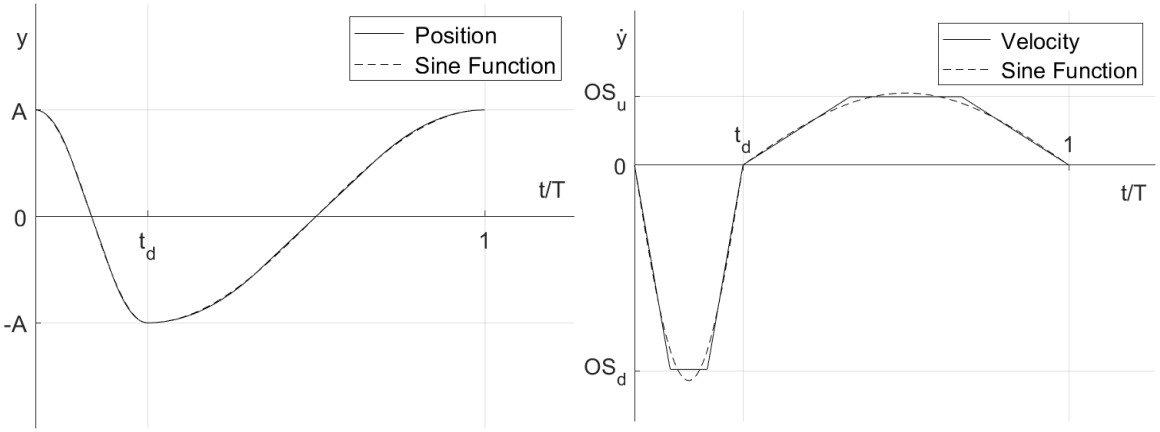

(a) Position as a function of period fraction for an asymmetric motion.

(b) Velocity as a function of period fraction for a symmetric motion.

Figure 3.17: Asymmetrical motion profile.

The speed values to be loaded in the MEXE02 software were obtained through an Excel spreadsheet. Some values were kept constant during the experimental process, and others changed according to the conditions to be tested. Airfoil chord ($c = 0.20\,\mathrm{m}$), and Reynolds number ($\mathrm{Re} = 1 \times 10^4$) were maintained constant during the whole experiment. Temperature and pressure were monitored throughout the experimental work, and are used to calculate fluid properties such as density and dynamic viscosity using the ideal gas and Sutherland's laws, respectively. The flow velocity at the exit of the wind tunnel was obtained through the

Reynolds number. The values of plunging cycle asymmetry, ζ, reduced frequency, k, and nondimensional amplitude, h, are modified for each experimental test, considering the parameter to be evaluated. Thus, the frequency, f, amplitude, A, and Strouhal number St are obtained through these parameters.

3.3 Experimental Validation

Before carrying out the experimental tests, it was necessary to verify that the motor was performing the desired motion. Thus, two motions were tested, one with equal and the other with unequal ascending and descending velocities.

The first motion has $\zeta = 0.5$, thus corresponding to a standard sinusoidal waveform. On the other hand, the second movement has asymmetric kinematics with $\zeta = 0.75$, meaning that the downward motion is performed faster than the upward one. After this and considering the linear actuator's limitations, the amplitude value was set to its maximum, with the frequency having a value close to the maximum allowed by the $0.8\,\mathrm{m\,s^{-1}}$ limit. So, the two conditions tested were:

- Condition 1: $\zeta = 0.5$, $A = 0.1\,\mathrm{m}$, $f = 1.00\,\mathrm{Hz}$
- Condition 2: $\zeta = 0.75$, $A = 0.1\,\mathrm{m}$, $f = 0.60\,\mathrm{Hz}$

After performing the two experimental tests, the airfoil's trailing-edge was tracked using Photron FASTCAM Viewer V4 software to obtain the airfoil's position in each frame. Figures 3.18a and 3.18b compare the experimental test with the desired motion. Thus, we observe that the linear actuator follows the desired motion.

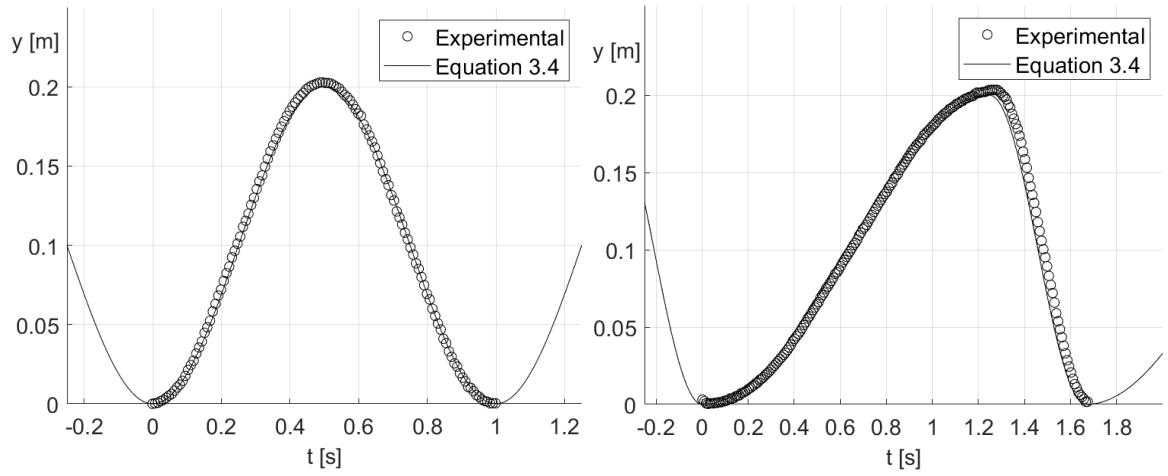

(a) Validation of condition 1.

(b) Validation of condition 2.

Figure 3.18: Comparison between the prescribed motion and experimental results.

Chapter 4

Results and Discussion

The fourth chapter of this dissertation presents the results of the experimental tests, as well as an analysis and discussion. This chapter is divided into four parts. The first consists of the presentation of the conditions that will be tested, and the following three in the analysis of the influence of the asymmetry parameter, ζ, reduced frequency, k, and nondimensional amplitude, h.

4.1 Tested Conditions

Since one of this work's primary objectives consists of analysing and comparing symmetric and asymmetric motions of a NACA0012 airfoil, several cases with different asymmetry parameters were tested. However, cases with different reduced frequencies and nondimensional amplitudes are also analysed since it is essential to understand the influence of these parameters too.

Four asymmetry parameter were considered, $\zeta = 0.5, 0.6, 0.7, 0.8$, and then the nondimensional amplitude values were chosen. These values were defined taking into account the linear actuator limit, i.e., the dimensionless amplitude cannot exceed the value $h = 0.5$ in any of the study cases. It was established that for each value of the asymmetry parameter, three values of nondimensional amplitude were tested, $h = 0.125, 0.25, 0.5$, and for each of these values, five reduced frequencies, $k = 0.5, 1, 2, 4, 8$.

As already stated in the previous chapter, it was verified if all these cases could be tested, i.e., if the speed limits of the motor stipulated by the manufacturer would not be exceeded. In this way, Table A.1 (Appendix A) makes a summary of all the cases intended to be studied. In this table, the speed values in both the upward and downward motion are observed, making it possible to verify if all cases can be studied. The table shows in red the speed values exceeding the maximum motor limit of $800\,\mathrm{mm\,s^{-1}}$.

The graph in Figure 4.1 illustrates Table A.1 as it shows which conditions may or may not be tested. The lines for the limit of the motor and linear actuator are plotted for each one of the conditions for different asymmetry values. The horizontal lines for $h = 0.5$ are the linear actuator's geometric limitations,and the parabolas define the kinematics limitations of the motor. The points represent the conditions plotted on the graph. Thus, the conditions on the left and below each line can be tested for that value of the asymmetry parameter. On the other hand, the conditions to the right and above cannot be tested for that ζ condition.

It is crucial to keep in mind that the curves obtained in Figure 4.1 for the different values of the asymmetry parameter are obtained taking into account the conditions under which the experimental tests were performed, these being $T = 18\,^{\circ}\mathrm{C}$, $P = 926\,\mathrm{hPa}$, $\mathrm{Re} = 1 \times 10^4$, and $c = 0.2\,\mathrm{m}$.

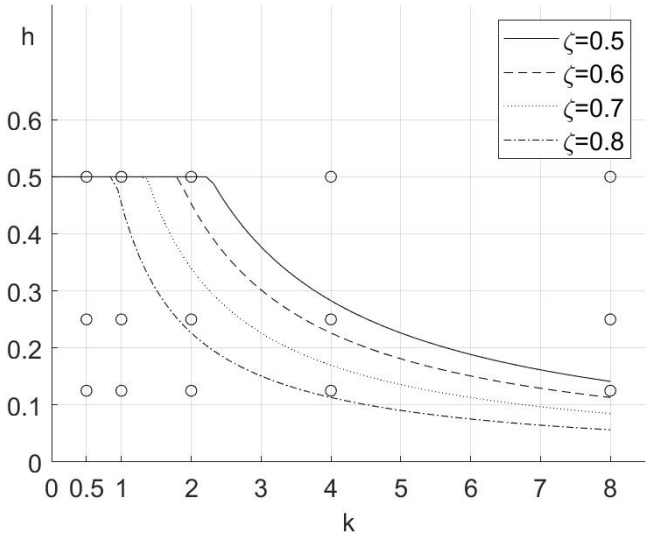

Figure 4.1: Motor limits and tested conditions.

After analysing the table, it is possible to observe the conditions that were tested according to the limits of the motor and linear actuator. Therefore, Table 4.1 was created to summarise the conditions that will be experimentally carried out.

Table 4.1: Final summary of the tested conditions.

ζ(t/T)	h	k
0.5	0.125	0.5
		1
		2
		4
		8
	0.25	0.5
		1
		2
		4
	0.5	0.5
		1
		2

ζ(t/T)	h	k
0.6	0.125	0.5
		1
		2
		4
	0.25	0.5
		1
		2
	0.5	0.5
		1

ζ(t/T)	h	k
0.7	0.125	0.5
		1
		2
		4
	0.25	0.5
		1
		2
	0.5	0.5
		1

ζ(t/T)	h	k
0.8	0.125	0.5
		1
		2
	0.25	0.5
		1
	0.5	0.5

4.2 Influence of the Asymmetry Parameter, ζ

4.2.1 Flow Visualization

In this subsection, the influence of the asymmetry parameter will be analysed, with visualisation and subsequent analysis of the airfoil wake structures for four different values of ζ, keeping, for each case, constant the values of nondimensional amplitude and reduced frequency.

Three cases are presented and studied below. Three values of nondimensional amplitude are presented, and for each one of them, the highest possible value of reduced frequency that is possible to study for all values of ζ, so that a comparison between all cases can be made. Thus, the presented cases are $h = 0.125$ and $k = 2$ (Figure 4.2), $h = 0.25$ and $k = 1$ (Figure 4.3) and finally, $h = 0.5$ and $k = 0.5$ (Figure 4.4). This means that the nondimensional velocity, kh, is the same for all cases.

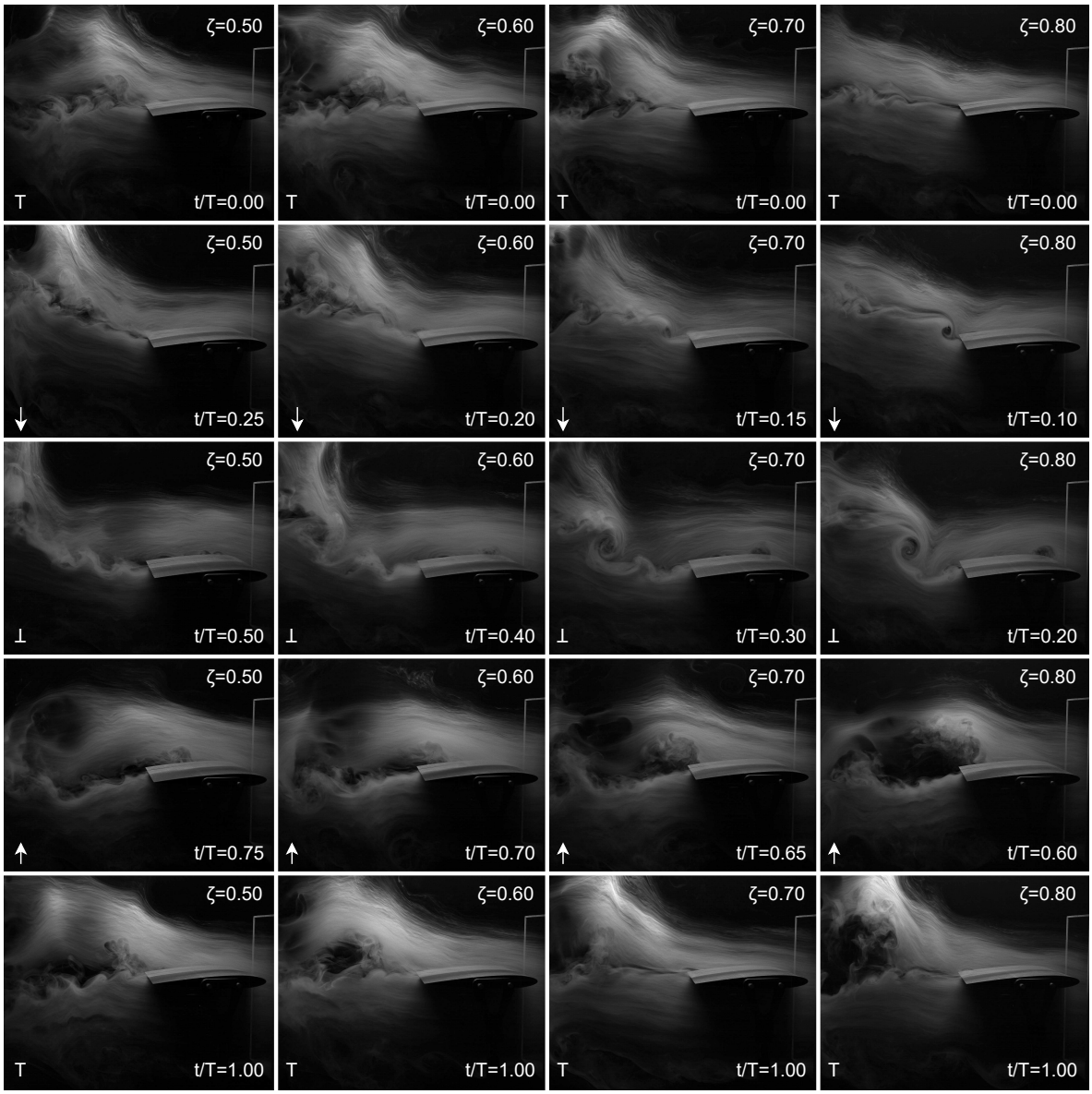

Figure 4.2: Flow visualization of $\zeta = 0.5, 0.6, 0.7$, and 0.8 with $h = 0.125$, and $k = 2$.

Each figure is composed of twenty images, whereby each column corresponds to a condition and each row to an airfoil position. Thus, the first, second, third and fourth columns represent the conditions $\zeta = 0.5, 0.6, 0.7$, and 0.8, respectively. Concerning the lines, each corresponds to a position of the airfoil. This means that for each figure, the first image corresponds to the beginning of the period, that is, to the highest position of the airfoil. In the second and third images, the airfoil is observed in the middle position of the downward

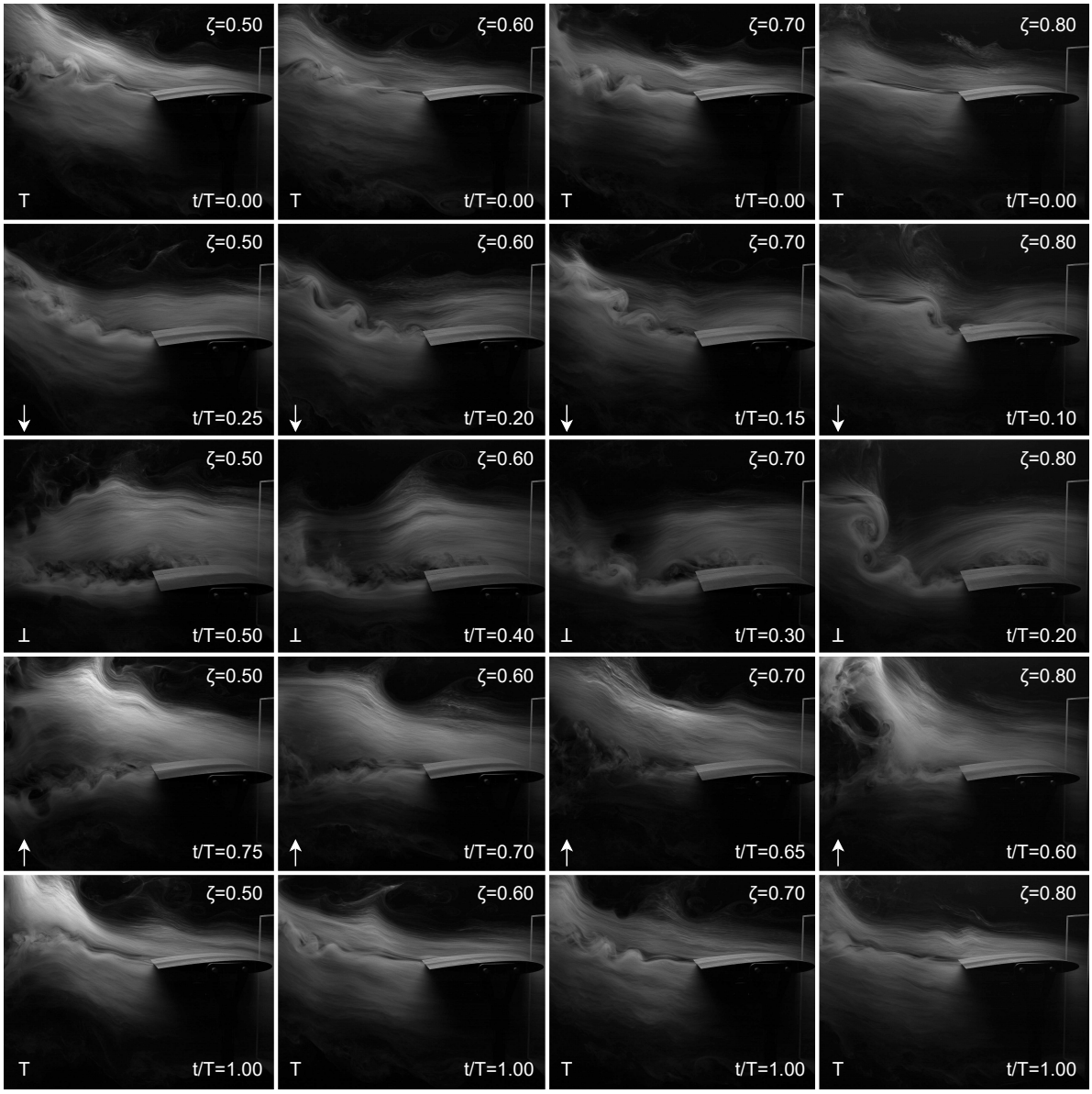

Figure 4.3: Flow visualization of $\zeta = 0.5, 0.6, 0.7$, and 0.8 with $h = 0.25$, and $k = 1$.

movement and its lowest position, respectively. Then, in the fourth image, the mid-position of the ascent, and in the fifth and last image, the airfoil is back to its upper position.

Considering the observation and analysis of the cases presented, it was found that despite the change in the values of nondimensional amplitude and reduced frequency, the influence of the parameter ζ is similar. This means that a general conclusion of the impact of the asymmetry parameter can be performed without taking into account the change in h and k values, which will be analysed later on.

When the airfoil is in its highest position, a detachment of the flow at the trailing-edge is observed in all cases. The formation of trailing-edge vortices in all cases is observed, noting that the increase of the asymmetry parameter also increases the size of these vortices.

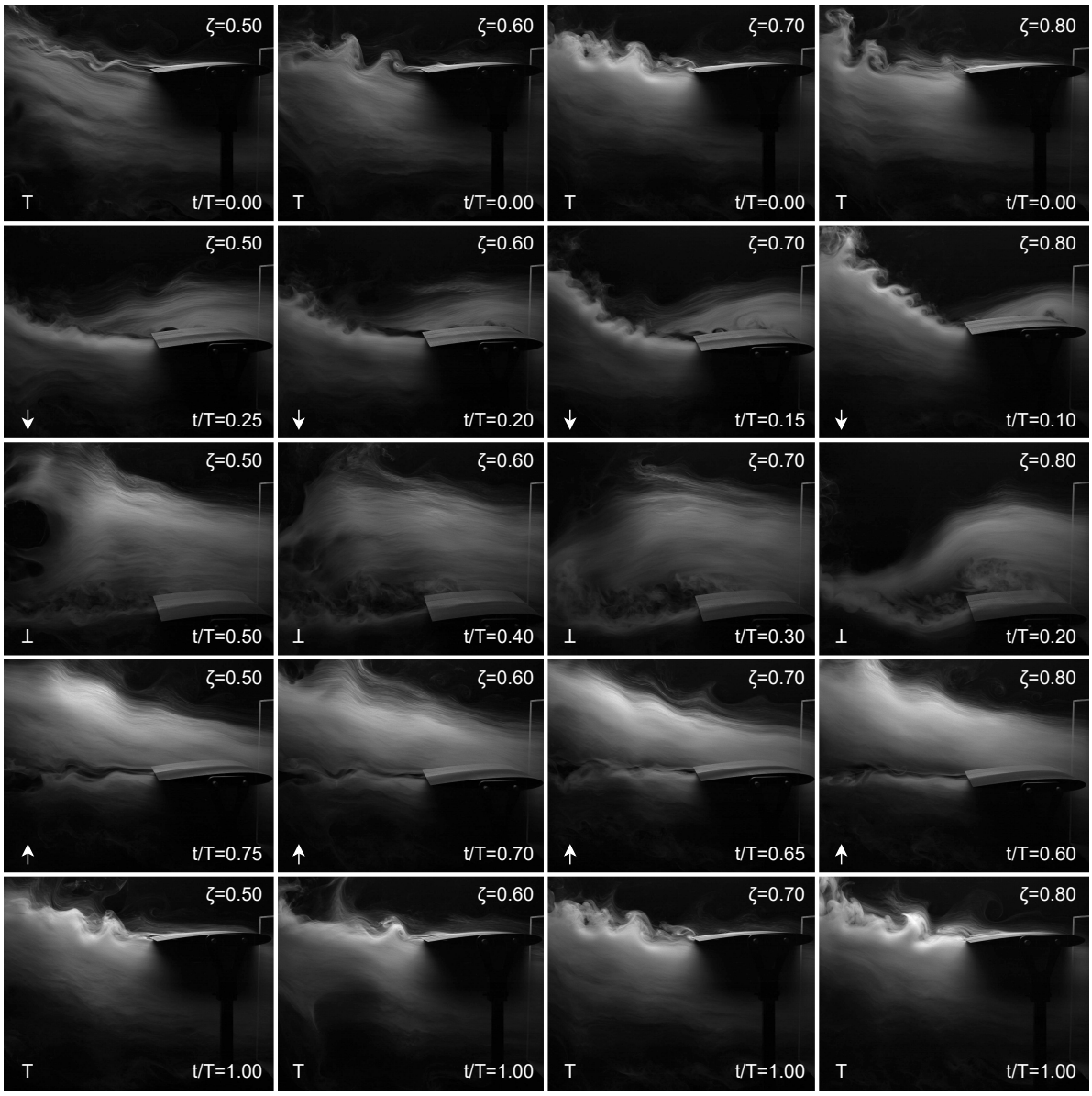

Figure 4.4: Flow visualization of $\zeta = 0.5$, 0.6, 0.7, and 0.8 with $h = 0.5$, and $k = 0.5$.

In the descent phase, leading-edge vortices appear, i.e. is identified separation of the flow. With increasing the asymmetry level, these vortices form earlier and become larger.

Arriving at its lower position, a zone of vorticity is observed on the airfoil's upper surface. As the motion asymmetry increases, these vortices are bigger and are found further upstream. Comparing the asymmetric case $\zeta = 0.6$ with the symmetric one, there is a difference in the inclination of the airfoil wake. This inclination increases with the increase of asymmetry, which indicates that there is an instantaneous production of thrust and lift for the asymmetric cases. With the rise of asymmetry, the production of the resultant aerodynamic force is expected to increase, since the tilt of the wake also increases.

During the ascending phase, it is verified for all cases that the flow is totally attached to the

airfoil surface, and no major differences are identified.

4.2.2 Influence on the effective angle of attack

An analysis of the effective angle of attack as a function of the period fraction was carried out for the three studied cases. In each case, four lines were drawn on the graphs below, thereby observing the effective angle of attack for each of the asymmetry levels, taking into account the condition considered. In Figure 4.5, the effective angle of attack is observed as a function of the period fraction for values of $h = 0.125$ and $k = 2$. In Figures 4.6 and 4.7, the same is represented, but in this case, for $h = 0.25$ and $k = 1$ and for $h = 0.50$ and $k = 0.50$, respectively. For all the conditions tested, flow visualization data was used to identify the time frames where the beginning of flow separation was observed. This phenomenon is identified by the points placed along the effective angle of attack profile.

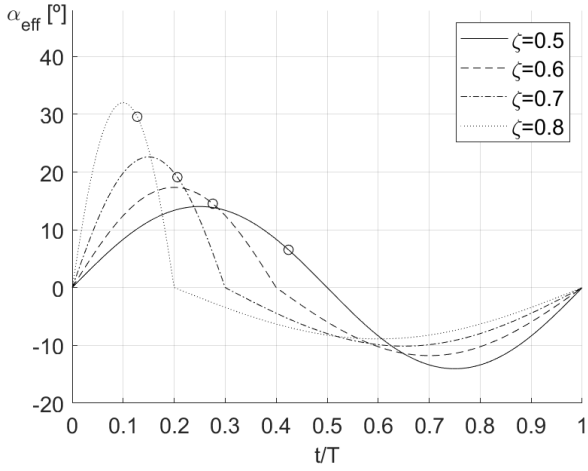

Figure 4.5: Effective angle of attack as a function of period fraction, for $h = 0.125$ and $k = 2$.

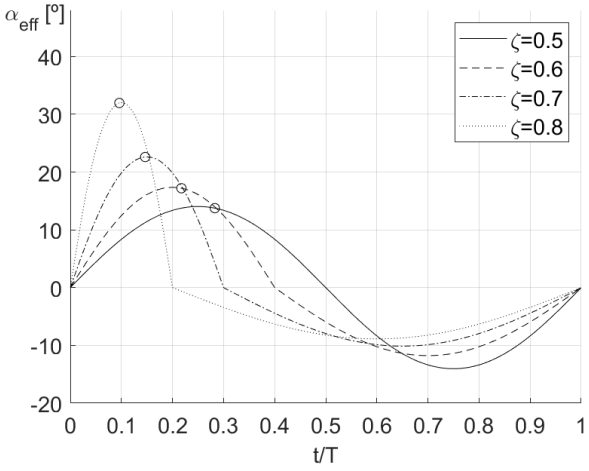

Figure 4.6: Effective angle of attack as a function of period fraction, for $h = 0.25$ and $k = 1$.

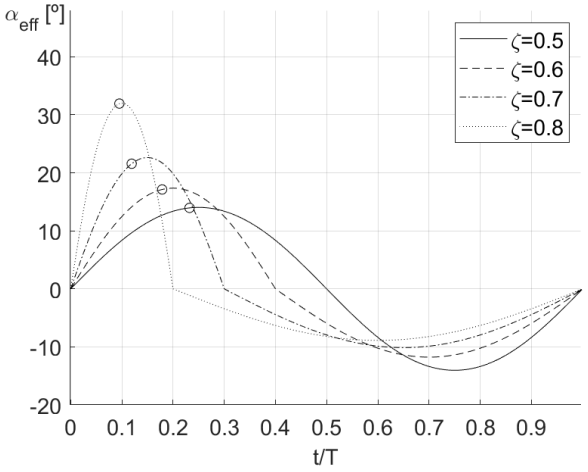

Figure 4.7: Effective angle of attack as a function of period fraction, for $h = 0.50$ and $k = 0.50$.

Although the effective angle of attack depends on the nondimensional amplitude and the reduced frequency, the curves remain the same for the identical asymmetry parameter in all graphs. This happens because every combination of h and k always results in the same nondimensional velocity, kh. For all cases of asymmetry, it is observed that the maximum

value of the effective angle of attack occurs halfway through the downward movement. In contrast, the lowest value occurs midway through the upward direction. It can be seen that the higher the level of asymmetry, the higher the maximum value of the effective angle of attack and the lower its minimum value. For any level of asymmetry, the separation of the flow always occurs in the downward phase of the motion. This means that for $\zeta = 0.5$, the separation occurs in the first half of the movement, for $\zeta = 0.6$ in the first 40%, for $\zeta = 0.7$ in the first 30% and finally, for $\zeta = 0.8$, in the first 20% of the period. Regarding the influence of the asymmetry of motion on the flow separation point, it is observed that the higher the value of ζ, the earlier the flow separation will occur, relative to the period fraction, being its effective angle of attack higher. In each of the three graphs, it is possible to observe a trend line deriving from the points where the beginning of flow separation at the leading-edge is observed. This trend starts at the point of flow separation when $\zeta = 1$ and $\alpha_{\text{eff}} = 90^\circ$ and extends until there is no more flow separation on the upper surface of the airfoil. In the graph of Figure 4.5, it is noticed that for any level of asymmetry, the flow separation begins after the maximum effective angle of attack. On the other hand, in Figure 4.6, it is observed that this phenomenon occurs near the maximum point of the effective angle of attack, and in Figure 4.7, it occurs before that point. Results show the complexity of prediction of flow separation on flapping airfoils, where there is not a single critical value of effective angle of attack that induces flow separation. So, it is concluded that the effective angle of attack by itself is not a reliable parameter to predict dynamic stall in these regimes.

4.3 Influence of the Nondimensional Amplitude, h

4.3.1 Flow Visualization

This section considers the influence of the nondimensional amplitude on the wake structures of a NACA0012 airfoil. In this way, three different values for this parameter will be compared, keeping the values of the asymmetry parameter and reduced frequency unchanged.

Four cases are shown, with each comparing the value of the nondimensional amplitude. Each one of the cases corresponds to a particular value of ζ and k. In this way, for each value of the asymmetry parameter, the largest value of reduced frequency was chosen, allowing a comparison between all values of h. Thus, the cases presented and studied below are $\zeta = 0.5$ and $k = 2$ (Figure 4.8), $\zeta = 0.6$ and $k = 1$ (Figure 4.9), $\zeta = 0.7$ and $k = 1$ (Figure 4.10), and $\zeta = 0.8$ and $k = 0.5$ (Figure 4.11).

Each of the four figures consists of fifteen images. Thus, each column corresponds to a value of h and each row to an airfoil position. Therefore, the columns represent $h = 0.125$, $h = 0.25$, and $h = 0.5$, respectively, from left to right. Regarding the rows, the first and fifth correspond to the start and end position of the period, which coincides with the highest position of the airfoil. The images of the second and fourth lines represent the airfoil in its downward and upward position, respectively. Finally, the third row corresponds to the position of the airfoil at mid-period, i.e., at its lowest position.

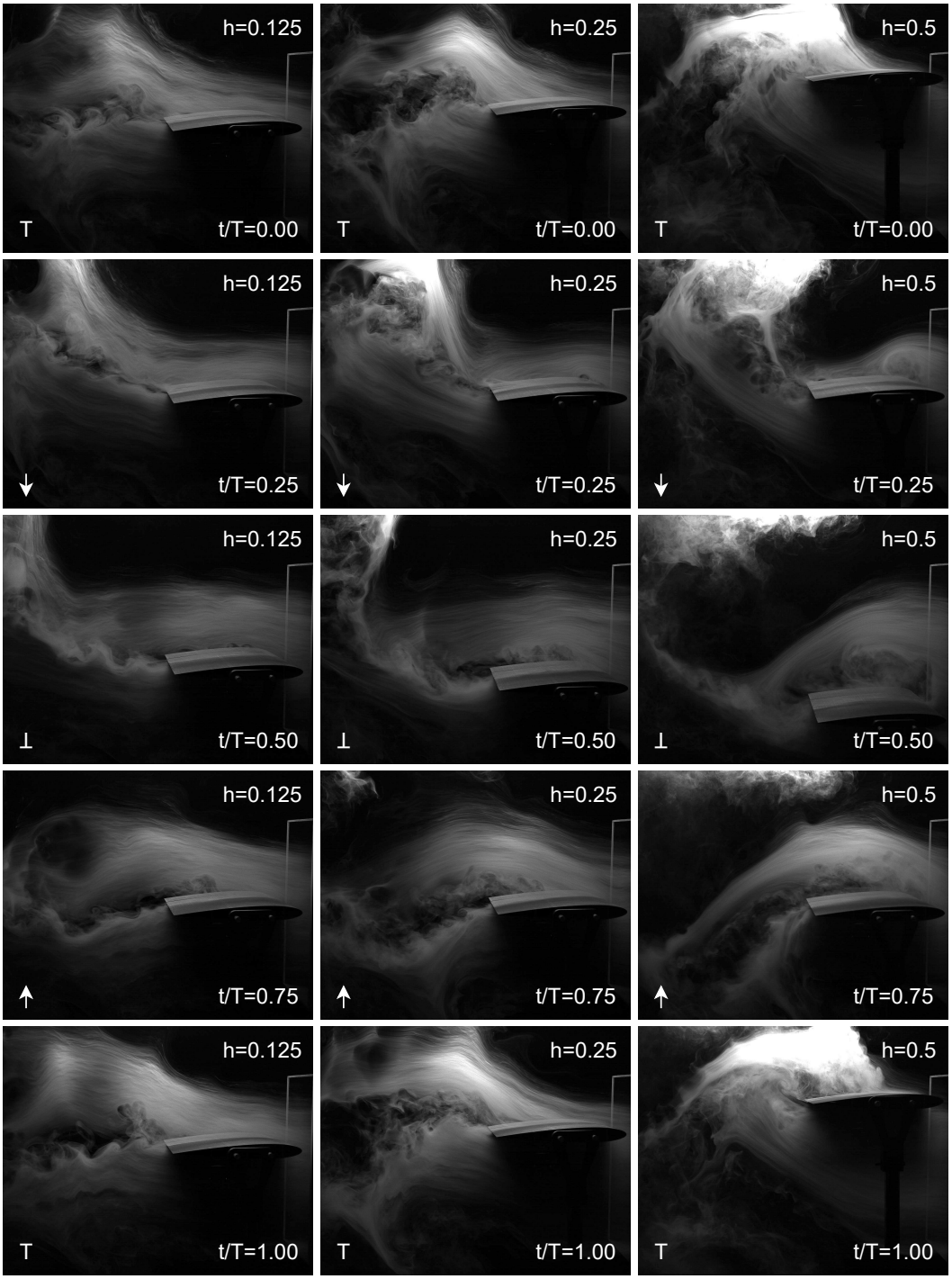

Figure 4.8: Flow visualization of $h = 0.125$, 0.25, and 0.5 with $\zeta = 0.5$, and $k = 2$.

Comparing the cases presented, it was observed that there are no significant changes in the influence of the nondimensional amplitude, despite the difference in the asymmetry parameter and the reduced frequency. Thus, it was decided to analyse all the cases together.

Starting by the analysis of the airfoil at its highest position, corresponding to the period's beginning, trailing-edge vortices are observed. These trailing-edge vortices form a von Kármán vortex street, which means that we are in the presence of a drag-producing wake. For the case where $h = 0.125$, the flow is totally attached to the airfoil's surface. However, as the

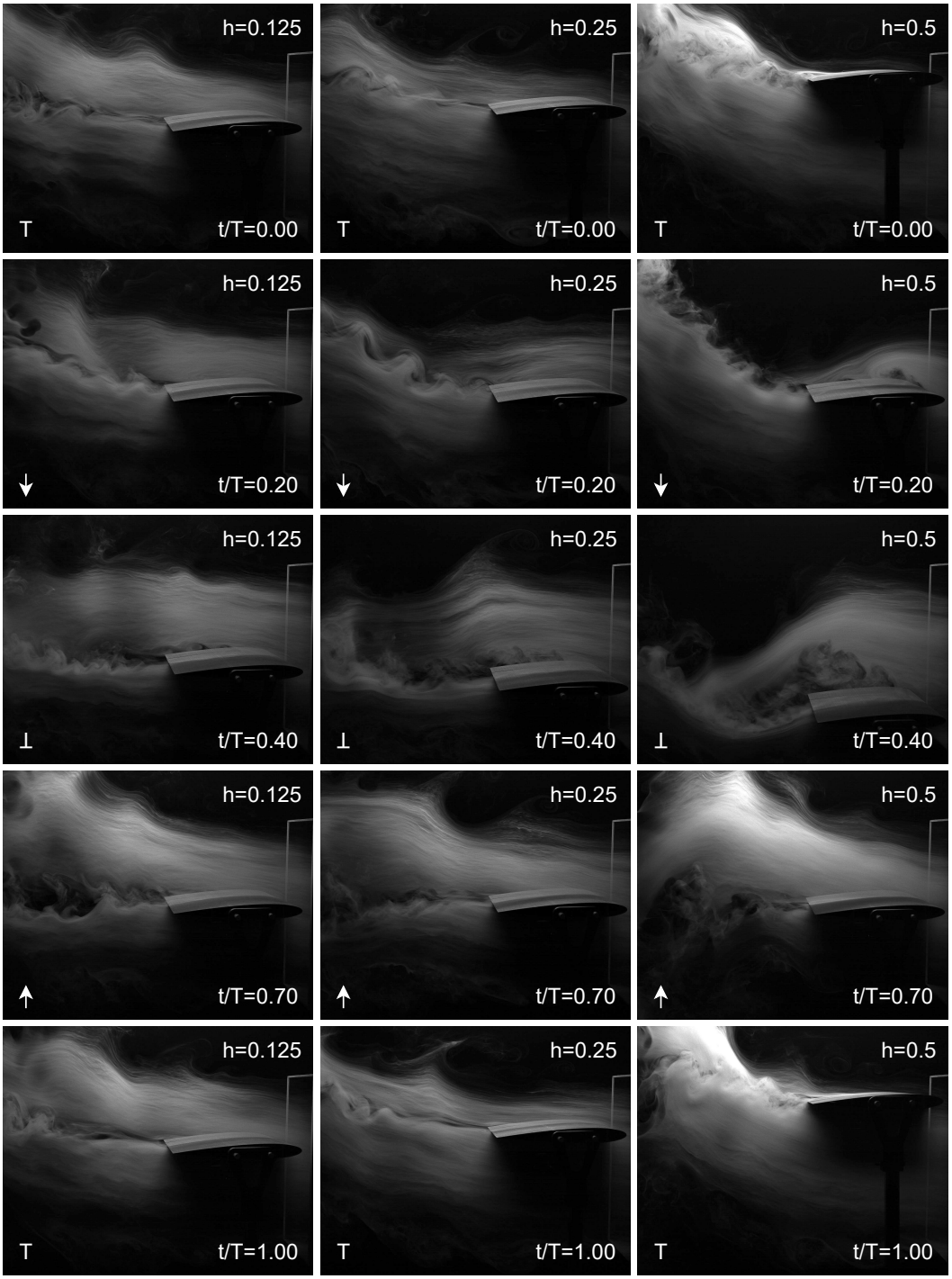

Figure 4.9: Flow visualization of $h = 0.125$, 0.25, and 0.5 with $\zeta = 0.6$, and $k = 1$.

parameter h increases, the flow detaches at the trailing-edge of the airfoil.

As the airfoil starts its downward motion, the trailing-edge vortices are larger in size. With increasing nondimensional amplitude, these trailing-edge vortices form in larger quantities and are more significant in terms of size. For the cases where $h = 0.125$, the flow is fully bonded to the airfoil's upper surface. However, with the increase of the parameter h, the appearance of leading-edge vortices is seen, as well as their size increase.

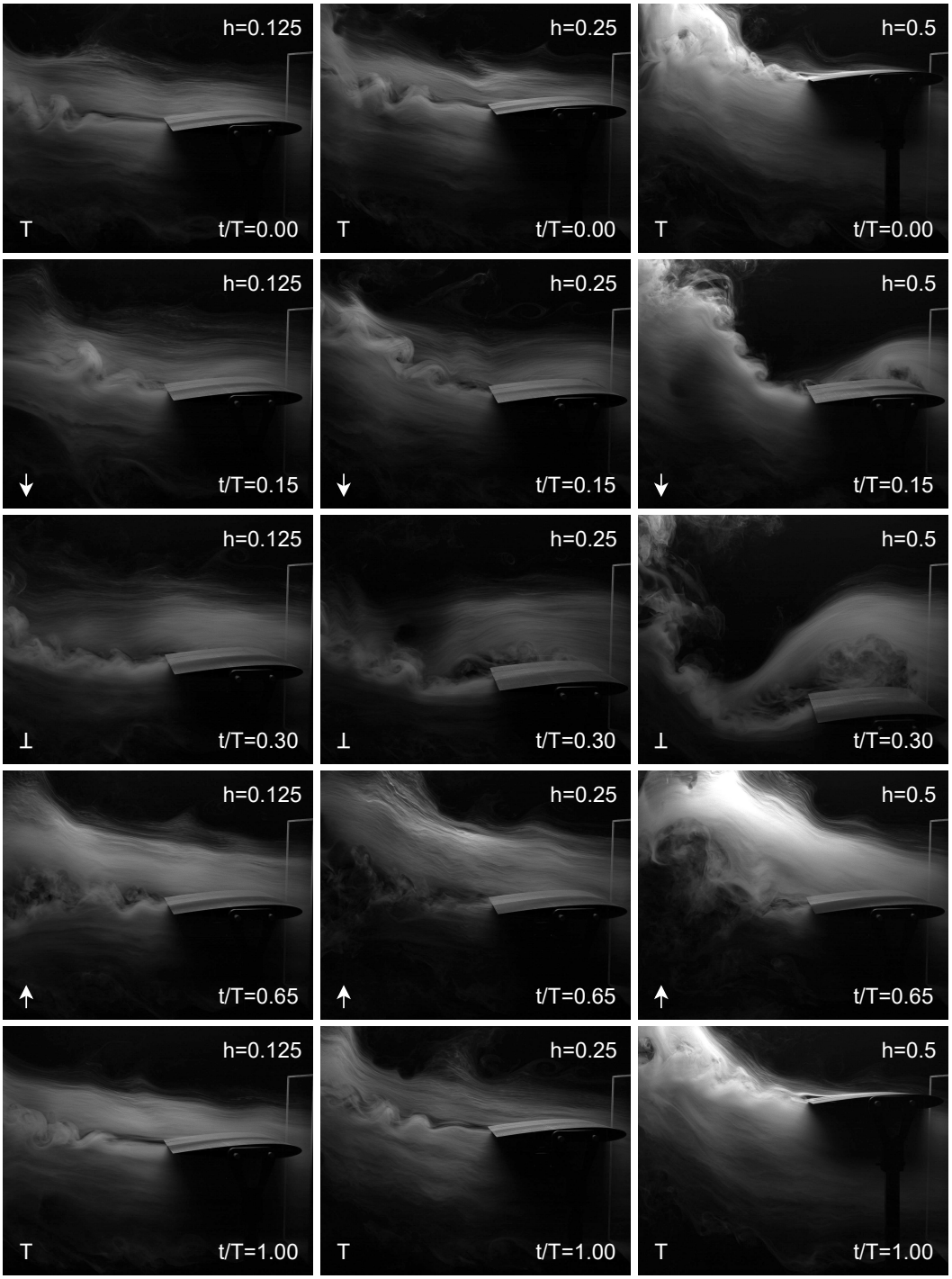

Figure 4.10: Flow visualization of $h = 0.125$, 0.25, and 0.5 with $\zeta = 0.7$, and $k = 1$.

In the middle of the motion period, or in other words, at the lowest position, there is an increase in the size of the leading-edge vortices in relation to the previous position. Thus, it can be seen that with the increase of the nondimensional amplitude, the vortices' size also increased, being formed more upstream. For the largest nondimensional amplitude, $h = 0.5$, it is observed that the leading-edge vortices occupy the entire upper surface of the airfoil. With the change of the parameter h, there is also a change in the wake size and the vertical distance of the trailing-edge vortices. This distance increases with the increase of the nondimensional

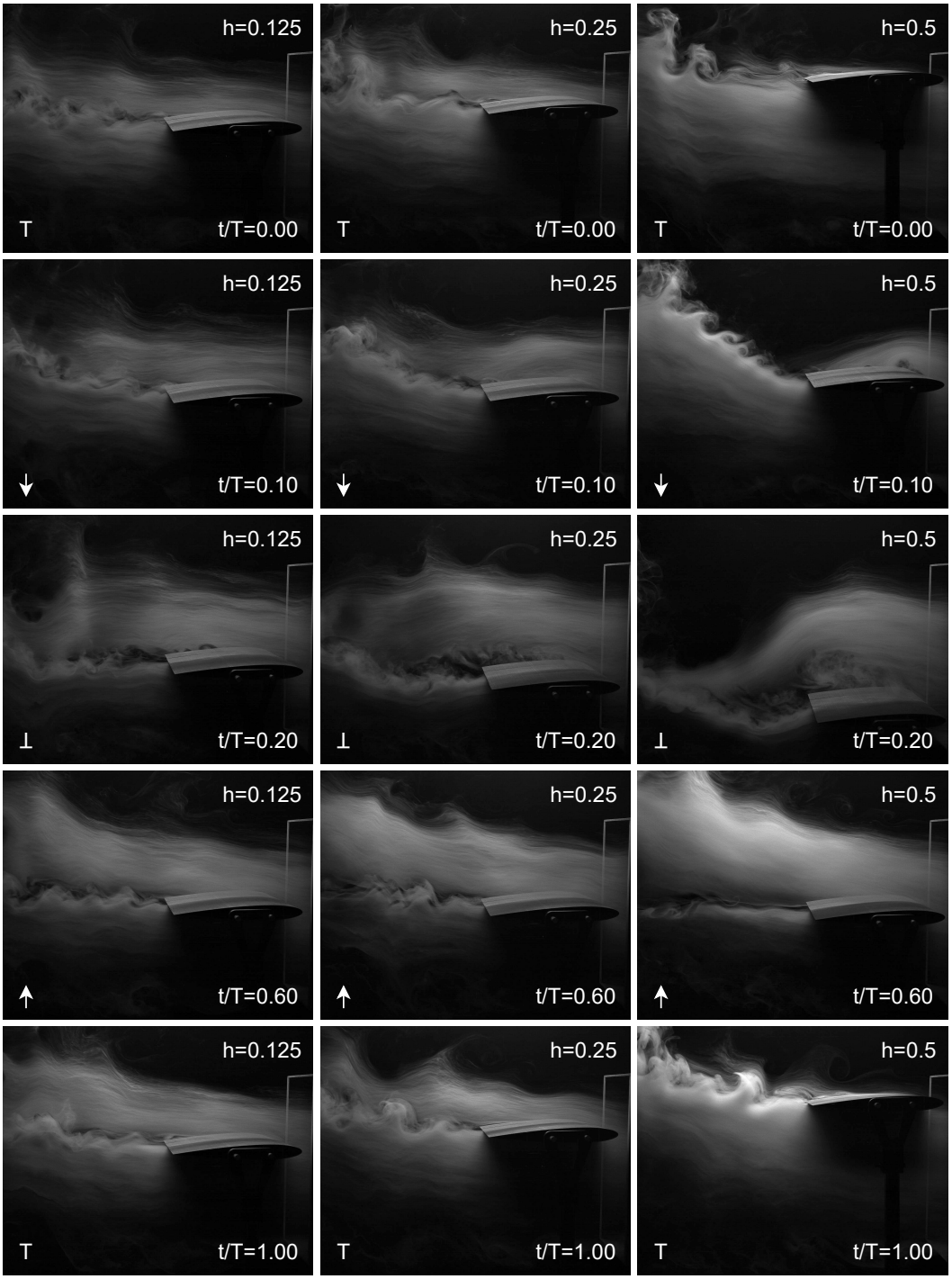

Figure 4.11: Flow visualization of $h = 0.125$, 0.25, and 0.5 with $\zeta = 0.8$, and $k = 0.5$.

amplitude.

In the upward movement of the airfoil, it is found that the leading-edge vortices formed earlier move to the trailing-edge, and the flow eventually sticks entirely to the top surface of the airfoil.

Finally, arriving at the final position, it can be seen that there are no significant differences concerning the beginning of the period.

4.3.2 Influence off the effective angle of attack

Next, the effective angle of attack is presented as a function of the period fraction for the four study cases. The three nondimensional amplitude values considered, $h = 0.125$, $h = 0.25$, and $h = 0.5$, are analysed in each case. In this way, four graphs are plotted, and in each one, a curve corresponding to each of the nondimensional amplitude values is drawn. Thus, Figure 4.12 presents the variation of the effective angle of attack as a function of the period fraction for $\zeta = 0.5$ and $k = 2$. Figures 4.13 and 4.14 correspond to values for $\zeta = 0.6$ and $k = 1$ and for $\zeta = 0.7$ and $k = 1$, respectively. Finally, Figure 4.15 presents the curves for $\zeta = 0.8$ and $k = 0.5$. By observing the flow visualisation data, it was possible to identify, for each case, the onset of flow separation at the airfoil's leading-edge. This separation is presented using the points drawn along the effective angle of attack curves in the graphs below.

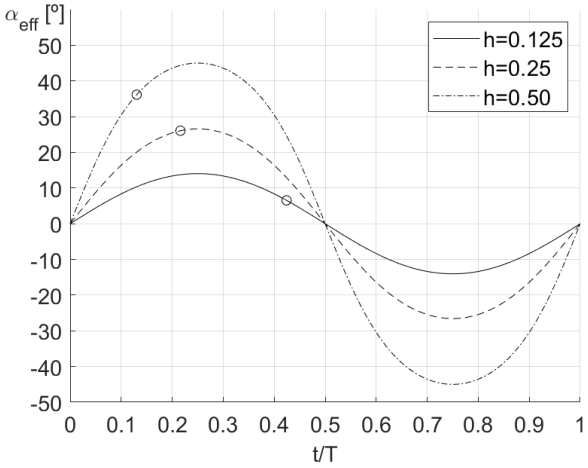

Figure 4.12: Effective angle of attack as a function of period fraction, for $\zeta = 0.5$ and $k = 2$.

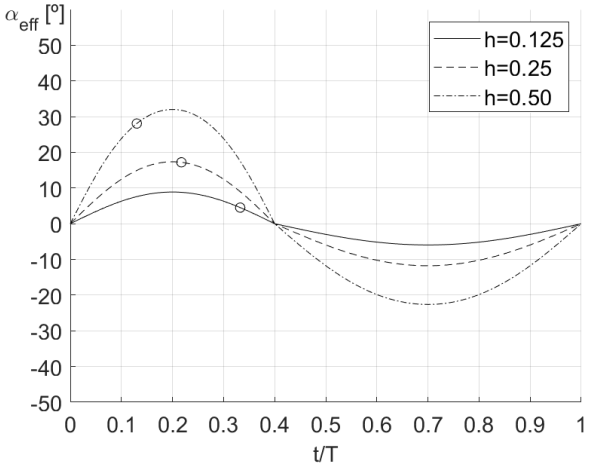

Figure 4.13: Effective angle of attack as a function of period fraction, for $\zeta = 0.6$ and $k = 1$.

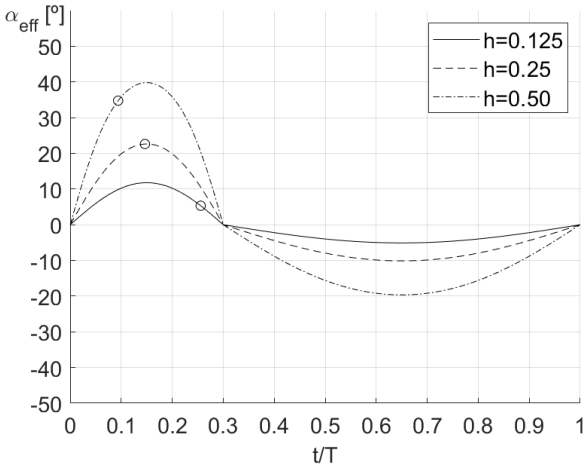

Figure 4.14: Effective angle of attack as a function of period fraction, for $\zeta = 0.7$ and $k = 1$.

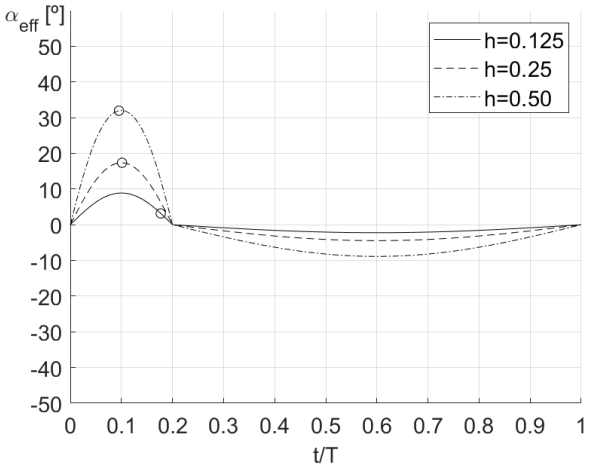

Figure 4.15: Effective angle of attack as a function of period fraction, for $\zeta = 0.8$ and $k = 0.5$.

With an increase in nondimensional amplitude, it is also observed an increase in the effective angle of attack. For the largest value of nondimensional amplitude, $h = 0.50$, the effective angle of attack is the highest in the first half of the period and the lowest in the second half, being the opposite observed for the lower nondimensional amplitude, $h = 0.125$. It is also

found, for all cases, that the effective angle of attack reaches its maximum value in the middle of the airfoil descent and its minimum value in the middle of the ascent. Regarding the flow's separation point, it is observed that the higher the nondimensional amplitude, the earlier this separation will occur. This phenomenon is observed for all four cases. For each of the graphs, it is seen that for $h = 0.5$, the separation occurs before the maximum effective angle of attack, for $h = 0.25$, it happens close to this maximum point, and finally, for $h = 0.125$, separation occurs after the maximum effective angle of attack. In this way, a trend line is observed concerning the points where flow separation is observed at the leading edge. This line starts when the nondimensional amplitude has such a high value that flow separation occurs for $t/T = 0$ and ends for a minimal h value, where flow separation no longer occurs.

4.4 Influence of the Reduced Frequency, k

4.4.1 Flow Visualization

The influence of the reduced frequency on the wake structures of the airfoil is now analysed through the visualisation and comparison of three distinct conditions. In this way, the value of the reduced frequency will be varied, keeping constant the asymmetry parameter and the nondimensional amplitude.

Four cases are compared to analyse the reduced frequency's influence on the airfoil wake structures. Three reduced frequencies were studied, $k = 0.5$, $k = 1$, and $k = 2$. The values $k = 4$ and $k = 8$ will not be presented since it is not possible to study them for all levels of asymmetry. This means that it is not possible to perform a comparison of these reduced frequency values for all levels of asymmetry. Each of the ζ values will be studied, and for each of these, the largest h that allows the study of these three k values was chosen. Thus, the cases of study are $\zeta = 0.5$ and $h = 0.5$ (Figure 4.16), $\zeta = 0.6$ and $h = 0.25$ (Figure 4.17), $\zeta = 0.7$ and $h = 0.25$ (Figure 4.18), and $\zeta = 0.8$ and $h = 0.125$ (Figure 4.19).

Fifteen images compose each of the four figures corresponding to each condition. The figures are divided into rows and columns for easier comparison and analysis of the results. The columns correspond to each of the studied reduced frequency values, and the rows to an airfoil position in a fraction of the period. This means that the columns represent the values $k = 0.5$, $k = 1$, and $k = 2$. The first row corresponds to the beginning of the period, the highest airfoil position. In the second, the airfoil is in the middle of its downward movement, and in the third, it is already at the lowest position, in the middle of the period. Similarly, the fourth and fifth lines show the airfoil in its middle ascent position and at its highest point, respectively.

As for the analyses of the asymmetry parameter and the nondimensional amplitude, a general comparison will be made for the four cases presented. This will be performed since no significant differences are observed from one case to the other in the influence of the reduced frequency.

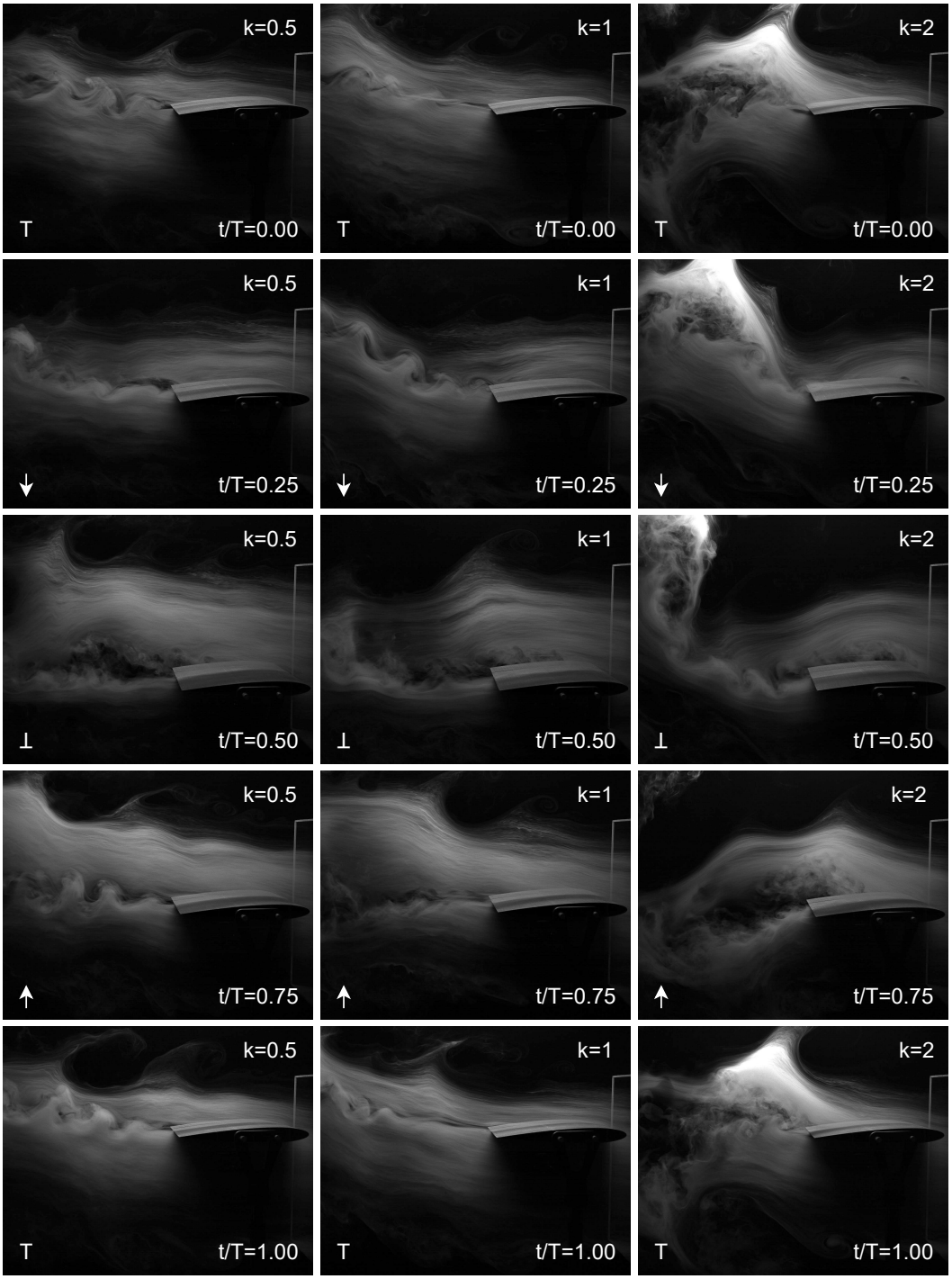

Figure 4.16: Flow visualization of $k = 0.5$, 1, and 2 with $\zeta = 0.5$, and $h = 0.5$.

When the airfoil is at the beginning of its motion, the formation of trailing-edge vortices is verified for all values of reduced frequency. However, as this parameter increases, the amount and size of these trailing edge vortices also increase. These sets of identified trailing-edge vortices form a typical von Kármán street. Thus, these are aerodynamic resistance vortices, which means that we are facing a drag-producing wake. The flow is fully attached to the airfoil upper surface in this motion position.

In the middle of its downward motion, trailing-edge vortices continue to be observed in the

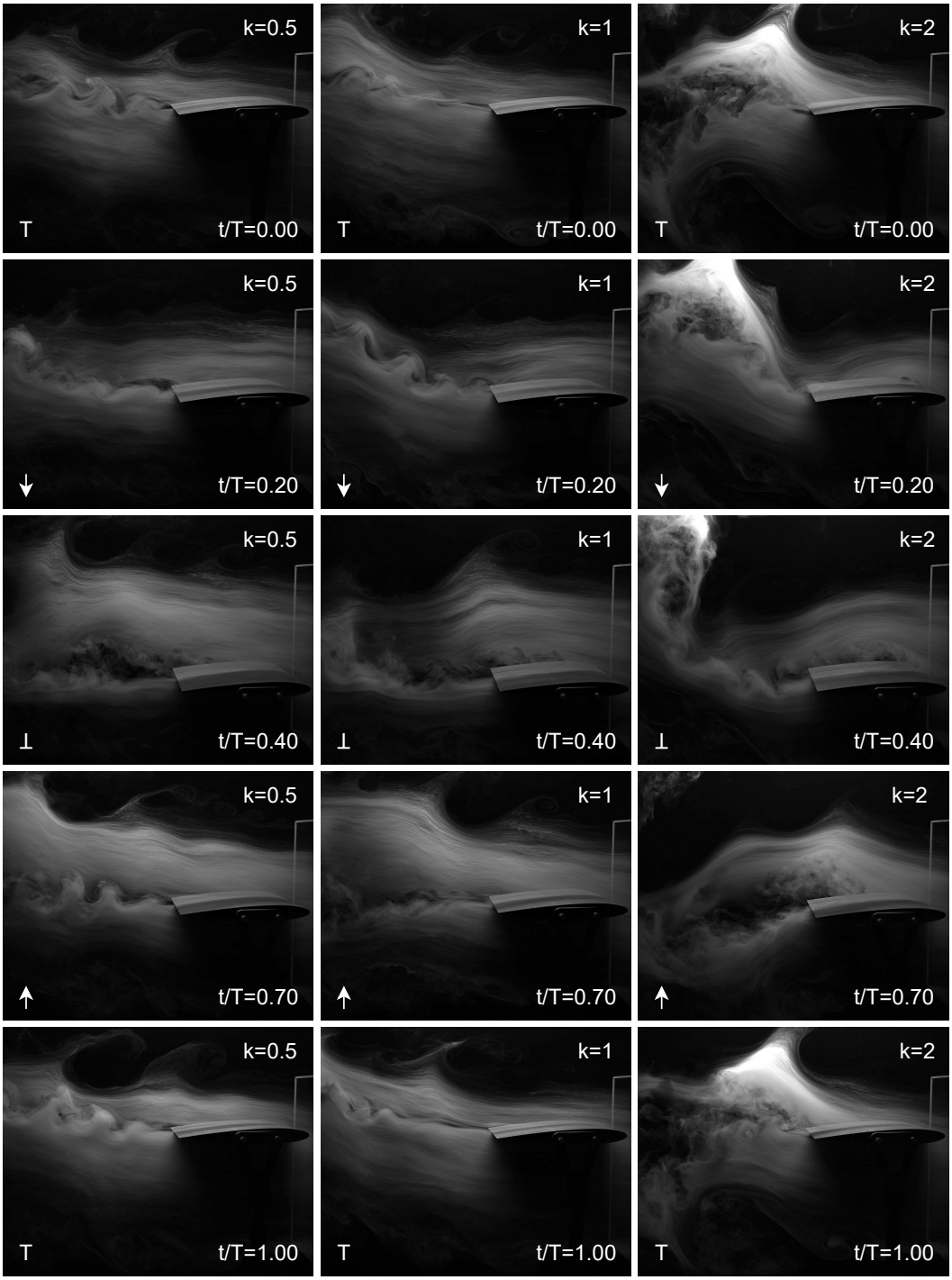

Figure 4.17: Flow visualization of $k = 0.5$, 1, and 2 with $\zeta = 0.6$, and $h = 0.25$.

wake of the airfoil. For reduced frequency values of $k = 0.5$ and $k = 1$, the flow is fully attached to the airfoil's upper surface. However, for $k = 2$, the formation of a leading edge vortex is observed.

Reaching the middle of the period, it is verified, as for the variation of the asymmetry parameter, that the wake is tilted, increasing with the increase of the reduced frequency. This means that the resultant aerodynamic force is composed not only by thrust but also by lift. Thus, the simultaneous production of thrust and lift increases with the increase of k, since

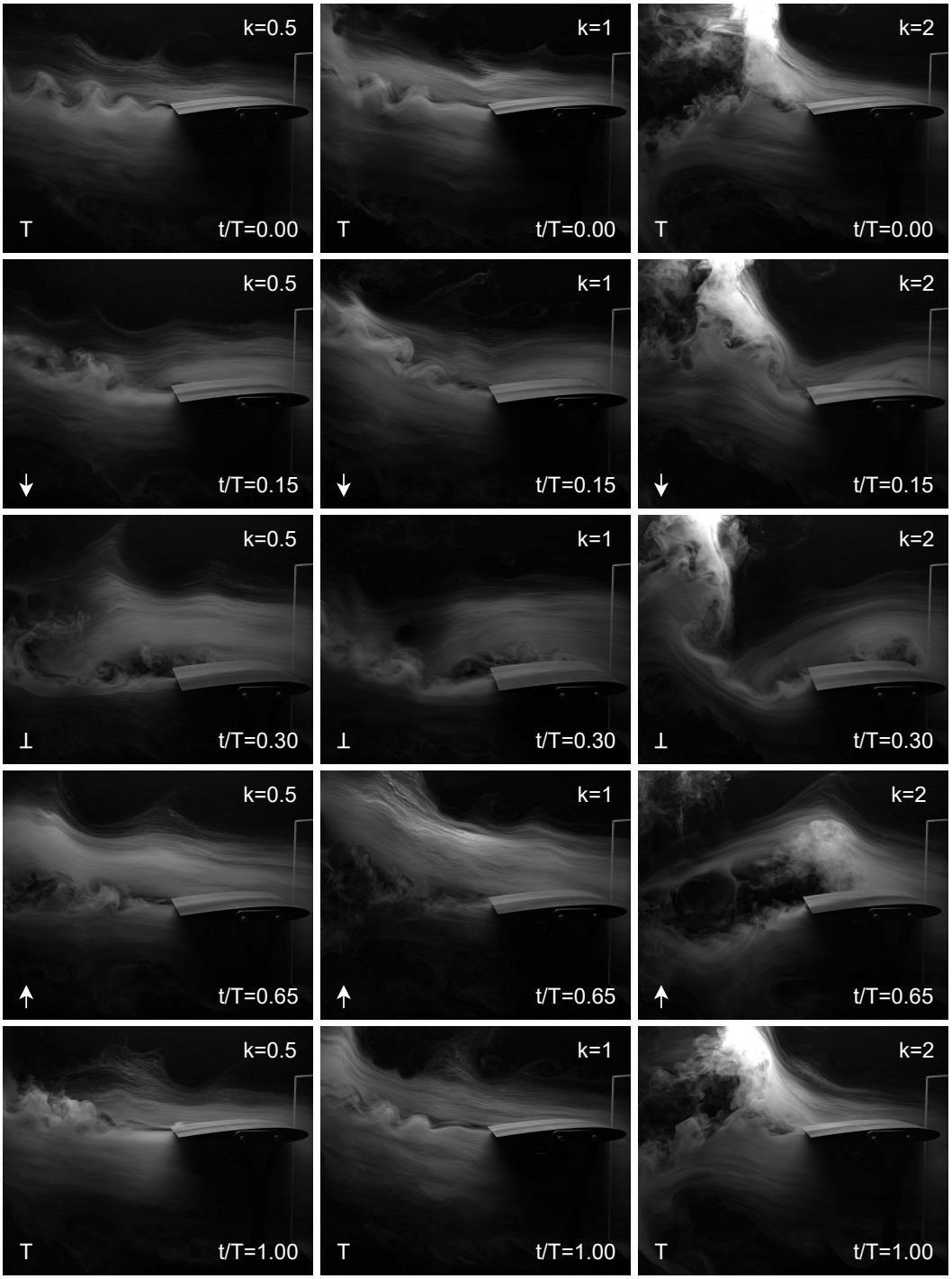

Figure 4.18: Flow visualization of $k = 0.5$, 1, and 2 with $\zeta = 0.7$, and $h = 0.25$.

the inclination of the wake also increases. It is also observed, at this position, a large amount of vortices on the airfoil's upper surface. As already observed for other airfoil positions, with increasing reduced frequency, leading-edge vortices have a larger size and form further upstream. It can be concluded that the reduced frequency affects the horizontal distance at which the vortices are released.

Halfway up the upward motion, the released leading-edge vortices are now on the trailing-edge of the airfoil. However, for higher values of reduced frequency, it is found that much

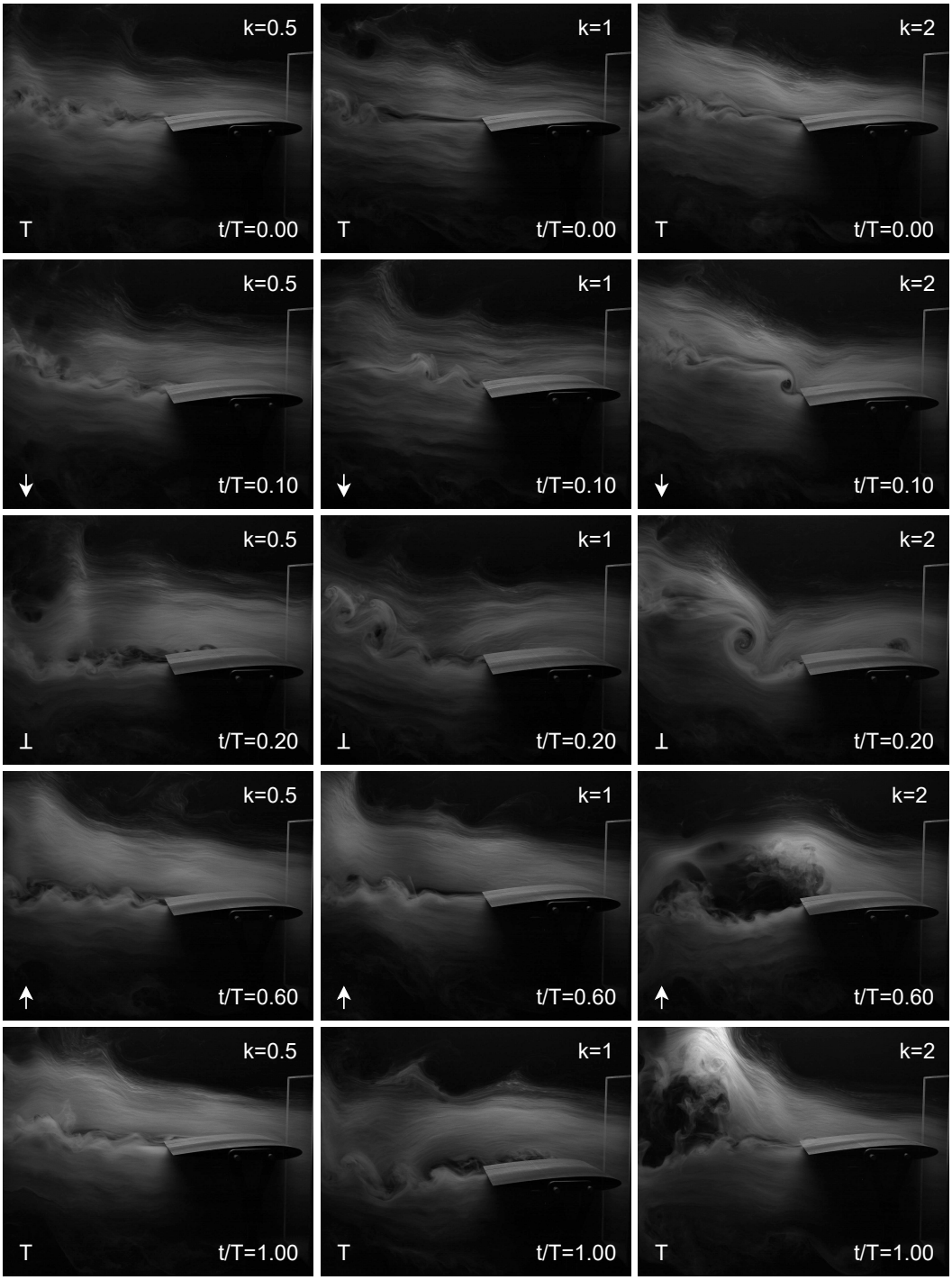

Figure 4.19: Flow visualization of $k = 0.5$, 1, and 2 with $\zeta = 0.8$, and $h = 0.125$.

of this vorticity formed at the leading-edge during descent is at the top of the airfoil. It is estimated that, for values even greater than $k = 2$, these vortices occupy the entire upper surface of the airfoil. Thus, for high values of reduced frequency, this phenomenon may indicate an energy extraction mechanism, and it may be possible to determine the magnitude of energy that the profile can extract from a free flow.

At the end of the movement, no significant differences are found in the airfoil compared to the initial position.

4.4.2 Influence of the effective angle of attack

The effective angle of attack as a function of the period fraction is presented for the four cases. Thus, for each case, three values of reduced frequency were analysed, $k = 0.50$, $k = 1$, and $k = 2$. Four graphs were then produced, with three curves, each corresponding to a reduced frequency value. In Figure 4.20 is represented the analysis of the effective angle of attack as a function of the period fraction, for $\zeta = 0.5$ and $h = 0.50$, while Figure 4.21 presents the same analysis but this time for $\zeta = 0.6$ and $h = 0.25$. Finally, Figures 4.22 and 4.23 correspond to values of $\zeta = 0.7$ and $h = 0.25$ and of $\zeta = 0.8$ and $h = 0.125$, respectively. This graph also shows, along each of the effective angle of attack curves, the flow separation point, for each of the cases under analysis. These points were obtained by observing the visualization data and represent where the beginning of flow separation at the leading-edge of the airfoil occurs.

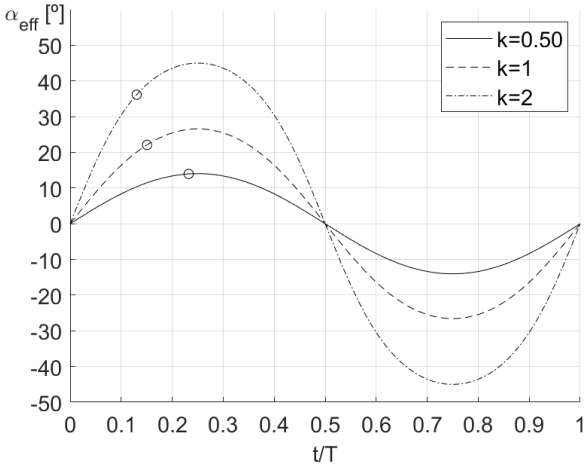

Figure 4.20: Effective angle of attack as a function of period fraction, for $\zeta = 0.5$ and $h = 0.50$.

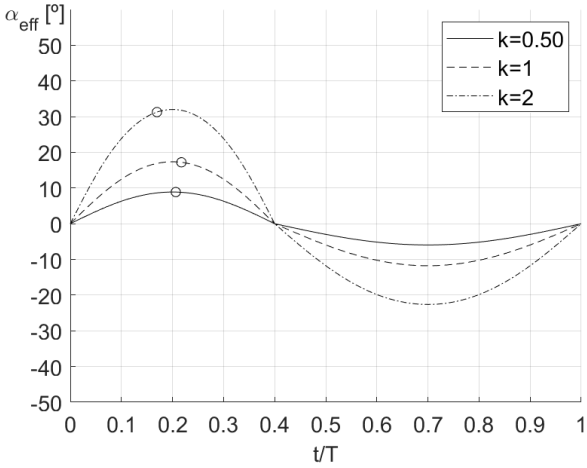

Figure 4.21: Effective angle of attack as a function of period fraction, for $\zeta = 0.6$ and $h = 0.25$.

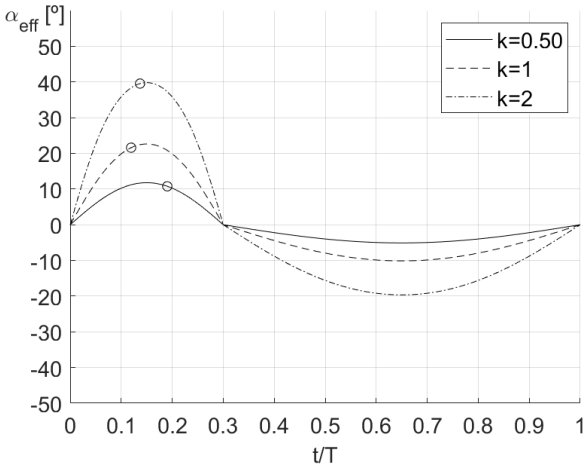

Figure 4.22: Effective angle of attack as a function of period fraction, for $\zeta = 0.7$ and $h = 0.25$.

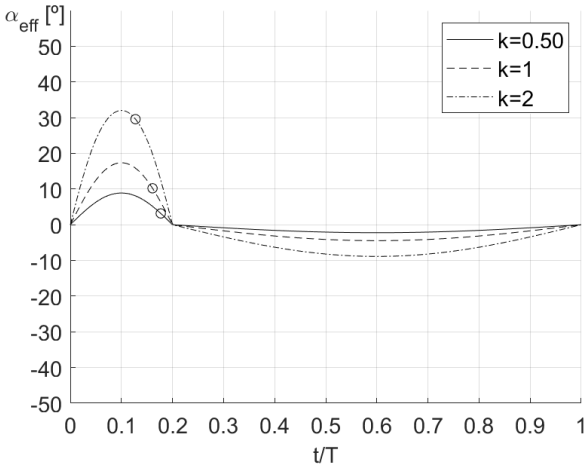

Figure 4.23: Effective angle of attack as a function of period fraction, for $\zeta = 0.8$ and $k = 0.125$.

It can be seen that as the reduced frequency increases, so does the effective angle of attack. Thus, the highest and lowest effective angle of attack values can be found for the highest value of reduced frequency, $k = 2$. It is also found that the largest effective angle of attack occurs

halfway down and the smallest value, halfway up, for all cases. Regarding the separation of the flow, it is seen that the point where this begins always occurs in the first part of the period, i.e. during the downward movement. For the case in which $\zeta = 0.5$, the flow separation occurs before the point of maximum effective angle of attack for all values of reduced frequency. On the other side, when $\zeta = 0.8$, the separation occurs after this point of maximum effective angle of attack. For the cases of Figures 4.20 and 4.23, a trend line is verified which unites the points where separation in the flow is observed. This line starts for the case having such a high value of reduced frequency that separation occurs at instant $t/T = 0$ and ends for a low value of k where no more separation occurs in the flow. Regarding the cases in Figures 4.21 and 4.22, the points where separation occurs in the flow do not follow the expected trend. This happens because in the case where $k = 1$, flow separation is observed after (Figure 4.21) or before (Figure 4.22) $k = 0.5$, which would not be expected.

Chapter 5

Conclusion

Since the dawn of time, animals moving in air or water have attracted the interest of researchers. The desire to fly emerged from the observation of birds, which culminated in the desire to replicate their type of locomotion. The animals that move in water and air have been investigated due to their type of locomotion that allows effective generation of thrust and lift at low Reynolds numbers. Thus, there has been great interest in replicating and developing these mechanisms to adapt them to the production of vehicles. Several studies have been developed in oscillating foils to understand which regimes offer the best results in terms of performance, efficiency and power harvesting. It has been found that replicating the wing flapping motion of birds is not simple, but over the years and with advances in research and technology, this problem has begun to be overcome. Several researchers have investigated pitching and plunging motions, separately and combined, to understand the generation of thrust and lift forces.

This dissertation continued the investigation of plunging airfoils, more specifically in asymmetric conditions. Through the analysis of the wake of a NACA0012 airfoil, the influence of motion asymmetry on wake patterns and structures was studied. The impact of other motion parameters, namely the nondimensional amplitude and the reduced frequency, was also considered.

In order to evaluate the influence of asymmetry level on the wake structures of NACA0012 airfoil, the asymmetry levels $\zeta = 0.5$, $\zeta = 0.6$, $\zeta = 0.7$, and $\zeta = 0.8$ were considered. For each of these asymmetry levels, three nondimensional amplitudes are studied, $h = 0.125$, $h = 0.25$, and $h = 0.5$. Finally, five reduced frequency values are considered for each of these nondimensional amplitudes, $k = 0.5$, $k = 1$, $k = 2$, $k = 4$, and $k = 8$. However, not all of these conditions can be tested due to the motor's and linear actuator's kinematic limits. A study of the effective angle of attack was also performed, observing the point where the starting of flow separation occurs at the leading edge of the airfoil, for each case study.

The study of the asymmetry of motion showed quite interesting conclusions. Through the results obtained, it was verified that for the asymmetry cases, there is a simultaneous production of thrust and lift, which does not occur in the symmetric case. In general, it is observed that the vortices formed both at the leading and trailing-edge have greater intensity for the cases in which there is asymmetry. It is also observed that this intensity increases with the increase of the asymmetry parameter. The maximum effective angle of attack increases with the increase of asymmetry. The flow separation occurs during the downward movement of

the airfoil in all cases. Finally, it is also found that the higher the asymmetry, the earlier the flow separation occurs. In this way, a trend line was verified in relation to the points where the initiation of flow separation is detected.

The influence of nondimensional amplitude on the wake patterns of the NACA0012 airfoil was analysed. A typical von Kármán vortex street was observed, which means the existence of a drag-producing wake. For higher values of nondimensional amplitude, the beginning of flow separation is seen near the leading-edge. With an increase in h, the size of these vortices also increases, and their formation begins more upstream. Nondimensional amplitude is a parameter that influences the vertical distance of the trailing-edge vortices shedding. This distance also increases with an increase in h. The maximum value of the effective angle of attack always occurs for higher nondimensional amplitude and flow separation occurs in the downstream phase of the airfoil motion for any value of nondimensional amplitude. For larger values of h, the flow separation occurs earlier. This means that we are in the presence of a trend line concerning the values where the beginning of flow separation is identified.

With the reduced frequency study, it was observed that the formation of trailing edge vortices is more intense for higher values of this parameter, as expected. Regarding the leading edge vortices, these are formed further upstream and have larger sizes as the reduced frequency increases. In this way, the reduced frequency influences the horizontal distance at which the vortices are released. Parameter k also affects the wake tilt. It was observed that an increase in reduced frequency will increase the wake inclination, meaning that we are not only in the presence of thrust production but also lift production. The maximum effective angle of attack value occurs for higher reduced frequencies, and the flow separation point is seen in the downward phase of the motion for all the cases. For two case studies, it is observed a trend line regarding the flow separation point. On the other hand, for the other two cases, this did not occur, which was not expected.

The study of airfoils with newer kinematics still requires much more studies and analysis, namely experimental studies. This is a fundamental topic in flapping wings since it may enable the discovery of new mechanisms that allow the simultaneous production of thrust and lift more effectively than those already studied. As future works, it is suggested the research and analysis of new kinematics and their influence on the wake structures and their deflection. The study of the effect of various parameters, such as the level of asymmetry, nondimensional amplitude and reduced frequency, should be expanded since these parameters influence the generation of thrust and lift and allow the existence of possible energy extraction mechanisms. The analysis of the influence of asymmetric sinusoidal motion on the flow's separation point is also a topic that still requires much attention and study.

Through the study conducted throughout this dissertation, a paper was written entitled "Investigation of Asymmetric Plunging of a NACA0012 Airfoil" [82] This paper was presented at the AIAA SciTech 2023.

Bibliography

[1] A. Vuruskan, I. Fenercioglu, and O. Cetiner, "A study on forces acting on a flapping wing," *EPJ Web of Conferences*, vol. 45, p. 01028, 2013. 1

[2] K. V. Rozhdestvensky and V. A. Ryzhov, "Aerohydrodynamics of flapping-wing propulsors," *Progress in Aerospace Sciences*, vol. 39, no. 8, pp. 585–633, nov 2003. 1

[3] W. Shyy, H. Aono, S. Chimakurthi, P. Trizila, C.-K. Kang, C. Cesnik, and H. Liu, "Recent progress in flapping wing aerodynamics and aeroelasticity," *Progress in Aerospace Sciences*, vol. 46, no. 7, pp. 284–327, oct 2010. 1

[4] M. F. Platzer, K. D. Jones, J. Young, and J. C. S. Lai, "Flapping wing aerodynamics: Progress and challenges," *AIAA Journal*, vol. 46, no. 9, pp. 2136–2149, sep 2008. 1

[5] R. Lopes, E. Camacho, F. Neves, A. R. R. Silva, and J. M. M. Barata, "Numerical and experimental study of a plunging airfoil," *Proceedings of the Thermal and Fluids Engineering Summer Conference*, p. 1869 – 1872, 2019. 2

[6] E. A. Camacho, F. Neves, J. Barata, and A. R. Silva, "Plunging airfoil: Reynolds number and angle of attack effects," *Energies*, vol. 13, no. 8, p. 1861, jun 2020. 2

[7] E. A. R. Camacho, F. M. S. P. Neves, A. R. R. Silva, and J. M. M. Barata, "Plunging airfoil: Reynolds number and angle of attack effects," *Aerospace*, vol. 8, no. 8, p. 216, aug 2021. 2

[8] E. A. Camacho, F. M. Neves, F. D. Marques, J. M. Barata, and A. R. Silva, "Effects of a dynamic leading edge on a plunging airfoil," *AIAA Aviation 2021 Forum and Exposition, Evento Online, EUA*, jul 2021. 2

[9] G. Torres, E. A. Camacho, F. D. Marques, and A. R. Silva, "Theoretical and numerical analysis of oscillating airfoil including viscous effects," *AIAA SciTech 2022 Forum and Exposition, Evento Hibrido, San Diego, CA, EUA*, jan 2022. 2

[10] R. Ferreira, E. A. Camacho, F. P. Neves, J. M. Barata, and A. R. Silva, "Wing design and analysis for micro air vehicle development," *AIAA SciTech 2022 Forum and Exposition, Evento Hibrido, San Diego, CA, EUA*, jan 2022. 2

[11] E. A. Camacho, F. D. Marques, A. R. Silva, and J. M. Barata, "Leading-edge parametric study of the NACA0012-IK30 airfoil," *2022 AIAA Aviation Forum Expositio, Chicago (IL), EUA*, jun 2022. 2

[12] S. B. Gonçalves, E. A. Camacho, and A. R. Silva, "Influence of trailing-edge shape on the propulsive performance of a plunging flat plate," *2022 AIAA Aviation Forum Expositio, Chicago (IL), EUA*, jun 2022. 2

[13] J. Pinho, E. A. R. Camacho, and A. R. R. Silva, "Design and testing of a wing with a morphing trailing edge," *2023 AIAA Aviation Forum Exposition, San Diego (CA), USA*, junho 2023. 2

[14] P. E. Fayemi, K. Wanieck, C. Zollfrank, N. Maranzana, and A. Aoussat, "Biomimetics: process, tools and practice," *Bioinspiration & Biomimetics*, vol. 12, no. 1, p. 011002, jan 2017. 3

[15] B. Bhushan, "Biomimetics: lessons from nature–an overview," *Philosophical Transactions of the Royal Society A: Mathematical, Physical and Engineering Sciences*, vol. 367, no. 1893, pp. 1445–1486, apr 2009. 3

[16] N. F. Lepora, P. Verschure, and T. J. Prescott, "The state of the art in biomimetics," *Bioinspiration & Biomimetics*, vol. 8, no. 1, p. 013001, jan 2013. 3

[17] J. Choi, J. Hwang, Y. Jeong, J. M. Park, K. H. Lee, and J. W. Hong, "Biomimetics: forecasting the future of science, engineering, and medicine," *International Journal of Nanomedicine*, p. 5701, sep 2015. 3

[18] C. D. Güss, S. Ahmed, and D. Dörner, "From da vinci's flying machines to a theory of the creative process," *Perspectives on Psychological Science*, vol. 16, no. 6, pp. 1184–1197, feb 2021. 3

[19] P. L. Richardson, "Leonardo da vinci's discovery of the dynamic soaring by birds in wind shear," *Notes and Records: the Royal Society Journal of the History of Science*, vol. 73, no. 3, pp. 285–301, oct 2018. 3

[20] F. E. C. Culick, "The wright brothers: First aeronautical engineers and test pilots," *AIAA Journal*, vol. 41, no. 6, pp. 985–1006, jun 2003. 4

[21] J. R. French and B. M. Ahmed, "The challenge of biomimetic design for carbon-neutral buildings using termite engineering," *Insect Science*, vol. 17, no. 2, pp. 154–162, apr 2010. 4

[22] J. F. V. Vincent, "Biomimetics — a review," *Proceedings of the Institution of Mechanical Engineers, Part H: Journal of Engineering in Medicine*, vol. 223, no. 8, pp. 919–939, sep 2009. 5

[23] Y. Bar-Cohen, "Biomimetics—using nature to inspire human innovation," *Bioinspira-*

tion & Biomimetics, vol. 1, no. 1, pp. P1–P12, mar 2006. 5

[24] L. Petricca, P. Ohlckers, and C. Grinde, "Micro- and nano-air vehicles: State of the art," *International Journal of Aerospace Engineering*, vol. 2011, pp. 1–17, 2011. 5

[25] K. D. Jones, T. C. Lund, and M. F. Platzer, "Experimental and computational investigation of flapping wing propulsion for micro air vehicles," pp. 307–339, jan 2001. 6

[26] T. A. Ward, M. Rezadad, C. J. Fearday, and R. Viyapuri, "A review of biomimetic air vehicle research: 1984-2014," *International Journal of Micro Air Vehicles*, vol. 7, no. 3, 2015. 6

[27] E. A. R. Camacho, "Numerical analysis of a plunging naca0012 airfoil," Master's thesis, Universidade da Beira Interior, 2019. 6

[28] X. Wu, X. Zhang, X. Tian, X. Li, and W. Lu, "A review on fluid dynamics of flapping foils," *Ocean Engineering*, vol. 195, p. 106712, jan 2020. 7

[29] G. C. Lewin and H. Haj-Hariri, "Modelling thrust generation of a two-dimensional heaving airfoil in a viscous flow," *Journal of Fluid Mechanics*, vol. 492, pp. 339–362, oct 2003. 8

[30] G. He, W. Mo, Y. Gao, Z. Zhang, J. Wang, W. Wang, P. Liu, and H. Ghassemi, "Modification of effective angle of attack on hydrofoil power extraction," *Ocean Engineering*, vol. 240, p. 109919, nov 2021. 8

[31] J.-S. Lee, C. Kim, and K. H. Kim, "Design of flapping airfoil for optimal aerodynamic performance in low-reynolds number flows," *AIAA Journal*, vol. 44, no. 9, pp. 1960–1972, sep 2006. 9

[32] R. Knoller and O. F. Verein, "Verlag des Österreichischer flugtechnischen vereines," *Die Gesetze des Luftwiderstandes*, 1909. 9

[33] A. Betz, "Ein beitrag zur erklärung des segelfluges," *Z Flugtech Motorluftschiffahrt*, 1912. 9

[34] K. Ohmi, M. Coutanceau, T. P. Loc, and A. Dulieu, "Vortex formation around an oscillating and translating airfoil at large incidences," *J. Fluid Mech.*, vol. 211, pp. 37–60, 1989. 9

[35] A. R. DAVARI, "Wake structure and similar behavior of wake profiles downstream of a plunging airfoil," *Chinese Journal of Aeronautics*, vol. 30, no. 4, pp. 1281–1293, aug 2017. 9, 10

[36] R. Katzmayr, "Effect of periodic changes of angle of attack on behavior of airfoils," *NACA Report 147*, 1922. 9

[37] K. D. Jones and M. F. Platzer, "Numerical computation of flapping-wing propulsion and power extraction," 1997. 9

[38] W. Birnbaum, "Das ebene problem des schlagenden flügels," *ZAMM - Zeitschrift für Angewandte Mathematik und Mechanik*, vol. 4, no. 4, pp. 277–292, 1924. 9

[39] K. D. Jones, B. M. Castro, O. Mahmoud, S. J. Pollard, M. F. Platzer, M. F. Neef, K. Gonet, and D. Hummel, "A collaborative numerical and experimental investigation of flapping-wing propulsion," 2002. 9

[40] T. von Kármán and Burgers, "General aerodynamic theory- perfect fluids," vol. 2, pp. 346–349, 1935. 10

[41] J. M. Anderson, K. Streitlien, D. S. Barrett, and M. S. Triantafyllou, "Oscillating foils of high propulsive efficiency," *Journal of Fluid Mechanics*, vol. 360, pp. 41–72, apr 1998. 10

[42] D. Rodrigues, E. A. Camacho, F. Neves, J. Barata, and A. R. Silva, "Plunging airfoil motion: Effects of unequal ascending and descending velocities," *AIAA AVIATION 2020 FORUM*, jun 2020. 10, 11, 12, 16, 19

[43] P. Freymuth, "Propulsive vortical signature of plunging and pitching airfoils," *AIAA Journal*, vol. 26, no. 7, pp. 881–883, jul 1988. 10

[44] K. D. Jones, C. M. Dohring, and M. F. Platzer, "Wake structures behind plunging airfoils - a comparison of numerical and experimental results," *American Institute of Aeronautics and Astronautics*, 1996. 11

[45] G. S. Triantafyllou, M. S. Triantafyllou, and M. A. Grosenbaugh, "Optimal thrust development on oscillating foils with appllication to fish propulsion," *Journal of Fluids and Structures*, 1992. 11

[46] I. E. Garrick, "Propulsion of a flapping and oscillating airfoil," *National Advisory Committee for Aeronautics*, 1936. 11

[47] T. Theodorsen, "General theory of aerodynamic instability and the mechanism of flutter," *National Advisoru Committee for Aeronautics 1940*, 1940. 11

[48] J. Pederzani and H. Haj-Hariri, "Numerical analysis of heaving flexible airfoils in a viscous flow," *AIAA Journal*, vol. 44, no. 11, pp. 2773–2779, nov 2006. 11

[49] M. J. Lighthill, "Aquatic animal propulsion of high hydromechanical efficiency," *J. Fluid Mech.*, 1970. 11

[50] S. Sarkar and K. Venkatraman, "Numerical simulation of incompressible viscous flow past a heaving airfoil," *International Journal for Numerical Methods in Fluids*, vol. 51, no. 1, pp. 1–29, 2006. 11

[51] J. C. S. Lai and M. F. Platzer, "Jet characteristics of a plunging airfoil," *AIAA Journal*, vol. 37, no. 12, pp. 1529–1537, dec 1999. 11

[52] J. Young, "Numerical simulation of the unsteady aerodynamics of flapping airfoils," Ph.D. dissertation, The University of New South Wales, 2005. 11

[53] J. Young and J. C. S. Lai, "Vortex lock-in phenomenon in the wake of a plunging airfoil," *AIAA Journal*, vol. 45, no. 2, pp. 485–490, feb 2007. 11

[54] J. B. Bratt, "Flow patterns in the wake of an oscillating aerofoil," *Aeronautical Research Council Reports and Memoranda*, 1953. 11

[55] K. D. Jones, C. M. Dohring, and M. F. Platzer, "Experimental and computational investigation of the knoller-betz effect," *AIAA Journal*, vol. 36, no. 7, pp. 1240–1246, jul 1998. 11

[56] N. H. Teng, "The development of a computer code for the numerical solution of unsteady , inviscid and incompressible flow over an airfoil," Master's thesis, U. S. Naval Postgraduate School, 1987. 11

[57] K. D. Jones and K. B. Center, "Numerical wake visualization for airfoils undergoing forced and aeroelastic motions," *34th Aerospace Sciences Meeting & Exhibit*, 1996. 11

[58] I. H. Tuncer and M. F. Platzer, "Thrust generation due to airfoil flapping," *AIAA Journal*, vol. 34, no. 2, pp. 324–331, feb 1996. 12

[59] I. Tuncer, R. Walz, and M. Platzer, "A computational study on the dynamic stall of a flapping airfoil," jun 1998. 12

[60] K. Isogai, Y. Shinmoto, and Y. Watanabe, "Effects of dynamic stall on propulsive efficiency and thrust of flapping airfoil," *AIAA Journal*, vol. 37, no. 10, pp. 1145–1151, oct 1999. 13

[61] R. Ramamurti and W. Sandberg, "Simulation of flow about flapping airfoils using finite element incompressible flow solver," *AIAA Journal*, vol. 39, no. 2, pp. 253–260, feb 2001. 13

[62] J. M. Anderson, “Vorticity control for efficient propulsion,” Ph.D. dissertation, Applied Ocean Science and Engineering, Massachusetts Inst. ofTechnology, Cambridge, 1996. 13

[63] G. K. Taylor, R. L. Nudds, and A. L. R. Thomas, “Flying and swimming animals cruise at a strouhal number tuned for high power efficiency,” *Nature*, vol. 425, no. 6959, pp. 707–711, oct 2003. 13

[64] J. Young and J. C. S. Lai, “Oscillation frequency and amplitude effects on the wake of a plunging airfoil,” *AIAA Journal*, vol. 42, no. 10, pp. 2042–2052, oct 2004. 13

[65] J. Young and J. Lai, “Mechanisms influencing the efficiency of oscillating airfoil propulsion,” *AIAA Journal*, vol. 45, no. 7, pp. 1695–1702, jul 2007. 13

[66] W. Geissler and B. G. van der Wall, “Dynamic stall control on flapping wing airfoils,” *Aerospace Science and Technology*, vol. 62, pp. 1–10, mar 2017. 13

[67] M. Yu, B. Wang, Z. Wang, and S. Farokhi, “Evolution of vortex structures over flapping foils in shear flows and its impact on aerodynamic performance,” *Journal of Fluids and Structures*, vol. 76, pp. 116–134, jan 2018. 14

[68] P. Luo, X. Zhang, P. Huang, and L. Xie, “A study on the aerodynamic characteristics of airfoil in the flapping adjustment stage during forward flight,” *Journal of Physics: Conference Series*, vol. 916, p. 012009, oct 2017. 14

[69] M. M. Koochesfahani, “Vortical patterns in the wake of an oscillating airfoil,” *AIAA Journal*, vol. 27, no. 9, pp. 1200–1205, sep 1989. 14

[70] Q. Xiao and W. Liao, “Numerical study of asymmetric effect on a pitching foil,” *International Journal of Modern Physics*, vol. 20, no. 10, 2009. 14

[71] K. Lu, Y. Xie, and D. Zhang, “Numerical study of large amplitude, nonsinusoidal motion and camber effects on pitching airfoil propulsion,” *Journal of Fluids and Structures*, vol. 36, pp. 184–194, jan 2013. 15

[72] K. Lu, Y. Xie, D. Zhang, and J. Lan, “Numerical investigations into the asymmetric effects on the aerodynamic response of a pitching airfoil,” *Journal of Fluids and Structures*, vol. 39, pp. 76–86, may 2013. 15

[73] Y. Zhang, R. S. Yuan, K. Lu, and Y. H. Xie, “Asymmetric sinusoidal motion effect on aerodynamics of a plunging airfoil,” *Advanced Materials Research*, vol. 712-715, pp. 1410–1413, jun 2013. 15

[74] L. Teng, J. Deng, D. Pan, and X. Shao, "Effects of non-sinusoidal pitching motion on energy extraction performance of a semi-active flapping foil," *Renewable Energy*, vol. 85, pp. 810–818, jan 2016. 16

[75] R. Sankarasubramanian, A. Sridhar, M. Prashanth, A. Mohammad, R. K. Velamati, and L. Vaitla, "Influence of thickness on performance characteristics of non-sinusoidal plunging motion of symmetric airfoil," *Aerospace Science and Technology*, vol. 81, pp. 333–347, oct 2018. 16

[76] G. L. Torres, E. A. Camacho, F. D. Marques, and A. R. Silva, "Simulations of a plunging airfoil undergoing unequal ascending and descending velocities at low reynolds numbers," jan 2021. 16

[77] K. Ramesh, A. Gopalarathnam, K. Granlund, M. V. Ol, and J. R. Edwards, "Discrete-vortex method with novel shedding criterion for unsteady aerofoil flows with intermittent leading-edge vortex shedding," *Journal of Fluid Mechanics*, vol. 751, pp. 500–538, jun 2014. 16

[78] M. Mekadem, T. Chettibi, H. Oualli, and S. Hanchi, "Thrust enhancement of a flapping airfoil using a non-sinusoidal motion trajectories," *Journal of the Brazilian Society of Mechanical Sciences and Engineering*, vol. 43, no. 4, mar 2021. 16

[79] R. B. de Sá Lopes, "Estudo dos padrões de vorticidade na esteira de uma asa em movimento de translação: Idealização e projeção de uma instalação experimental," Master's thesis, Universidade da Beira Interior, 2018. 19

[80] D. C. Rodrigues, "Visualização e análise das estruturas na esteira de um perfil naca0012 em movimento oscilatório vertical," Master's thesis, Universidade da Beira Interior, 2020. 19

[81] P. A. Castro, "Projecto e instalação de um túnel de vento para a realização do estudo experimental da interacção de um jacto de parede e uma camada limite," Master's thesis, Universidade da Beira Interior, 2004. 20

[82] J. G. Silva, E. A. Camacho, and A. R. Silva, "Investigation of asymmetric plunging of a NACA0012 airfoil," *AIAA SciTech 2023 Forum and Exposition, Evento Hibrido, National Harbor, MB, EUA*, jan 2023. 52

Appendix A

Anexes

A.1 Cases considered

Table A.1: Analysis of the conditions to be tested.

ζ(t/T)	h	k	f[Hz]	T[s]	A[mm]	OS_u[mm/s]	OS_d[mm/s]	St
0.5	0.125	0.5	0.2978	3.3577	25	44.3726	44.3726	0.0199
		1.0	0.5956	1.6788	25	88.7452	88.7452	0.0398
		2.0	1.1913	0.8394	25	177.4903	177.4903	0.0796
		4.0	2.3826	0.4197	25	354.9806	354.9806	0.1592
		8.0	4.7652	0.2099	25	709.9613	709.9613	0.3183
	0.25	0.5	0.2978	3.3577	50	88.7452	88.7452	0.0398
		1.0	0.5956	1.6788	50	177.4903	177.4903	0.0796
		2.0	1.1913	0.8394	50	354.9806	354.9806	0.1592
		4.0	2.3826	0.4197	50	709.9613	709.9613	0.31831
		8.0	4.7652	0.2099	50	1419.9225	1419.9225	0.6366
	0.5	0.5	0.2978	3.3577	100	177.4903	177.4903	0.0796
		1.0	0.5956	1.6788	100	354.9806	354.9806	0.1592
		2.0	1.1913	0.8394	100	709.9613	709.9613	0.3183
		4.0	2.3826	0.4197	100	1419.9225	1419.9225	0.6366
		8.0	4.7652	0.2099	100	2839.8451	2839.8451	1.2732
0.6	0.125	0.5	0.2978	3.3577	25	36.9771	55.4657	0.0199
		1.0	0.5956	1.6788	25	73.9542	110.9314	0.0398
		2.0	1.1913	0.8394	25	147.9086	221.8629	0.0796
		4.0	2.3826	0.4197	25	295.8172	443.7258	0.1592
		8.0	4.7652	0.2099	25	591.6344	887.4516	1.2732
	0.25	0.5	0.2978	3.3577	50	73.9543	110.9314	0.0398
		1.0	0.5956	1.6788	50	147.9086	221.8629	0.07958
		2.0	1.1913	0.8394	50	295.8172	443.7258	0.1592
		4.0	2.3826	0.4197	50	591.6344	887.4516	0.3183
		8.0	4.7652	0.2099	50	1183.2688	1774.9032	0.6366
	0.50	0.5	0.2978	3.3577	100	147.9086	221.8629	0.0796
		1.0	0.5956	1.6788	100	295.8172	443.7258	0.1592
		2.0	1.1913	0.8394	100	591.6344	887.4516	0.3183
		4.0	2.3826	0.4197	100	1183.2688	1774.9032	0.6366
		8.0	4.7652	0.2099	100	2366.5375	3549.8063	1.2732
0.7	0.125	0.5	0.2978	3.3577	25	31.6947	73.9543	0.0199
		1.0	0.5956	1.6788	25	63.3894	147.9086	0.0.0398
		2.0	1.1913	0.8394	25	126.7788	295.8172	0.0796
		4.0	2.3826	0.4197	25	253.5576	591.6344	0.1592
		8.0	4.7652	0.2099	25	507.1152	1183.2688	1.2732
	0.25	0.5	0.2978	3.3577	50	63.3894	147.9086	0.03979
		1.0	0.5956	1.6788	50	126.7788	295.8172	0.0796
		2.0	1.1913	0.8394	50	253.5576	591.6344	0.1592
		4.0	2.3826	0.4197	50	507.1152	1183.2688	0.3183
		8.0	4.7652	0.2099	50	1014.2304	2366.5375	0.6366

ζ(t/T)	h	k	f[Hz]	T[s]	A[mm]	OS_u[mm/s]	OS_d[mm/s]	St
0.7	0.50	0.5	0.2978	3.3577	100	126.7788	295.8172	0.0796
		1.0	0.5956	1.6788	100	253.5576	591.6344	0.1592
		2.0	1.1913	0.8394	100	507.1152	1183.2688	0.3183
		4.0	2.3826	0.4197	100	1014.2304	2366.5375	0.6366
		8.0	4.7652	0.2099	100	2028.4608	4733.0751	1.2732
0.8	0.125	0.5	0.2978	3.3577	25	27.7329	110.9314	0.0199
		1.0	0.5956	1.6788	25	55.4657	221.8629	0.0398
		2.0	1.1913	0.8394	25	110.9315	443.7258	0.0796
		4.0	2.3826	0.4197	25	221.8629	887.4516	0.1592
		8.0	4.7652	0.2099	25	443.7258	1774.9032	0.31831
	0.25	0.5	0.2978	3.3577	50	55.4657	221.8629	0.0398
		1.0	0.5956	1.6788	50	110.9314	443.7258	0.0796
		2.0	1.1913	0.8394	50	221.8629	887.4516	0.1592
		4.0	2.3826	0.4197	50	443.7258	1774.9032	0.3183
		8.0	4.7652	0.2099	50	887.4516	3549.8063	0.6366
	0.50	0.5	0.2978	3.3577	100	110.9314	443.7258	0.0796
		1.0	0.5956	1.6788	100	221.8629	887.4516	0.1592
		2.0	1.1913	0.8394	100	443.7258	1774.9032	0.3183
		4.0	2.3826	0.4197	100	887.4516	3549.8063	0.6366
		8.0	4.7652	0.2099	100	1774.9032	7099.6126	1.2732